Modeling mechanochemical coupling in cell polarity establishment

Ondrej Maxian

September 27, 2023

This project is about understanding the design principles by which cells combine mechanics (the actomyosin network) and biochemistry to robustly polarize.

1 Biochemistry of PAR-3 and PAR-2

We are motivated first by the experimental observations that asymmetries in the PAR proteins are stable once set up, even in the absence of contractility. This experimental observation tells us that there is an intrinsic bistability in the biochemical circuit, which switches from a uniform state to a polarized state. In later sections, the switch will occur under the influence of actomyosin flows, while in this section the initial conditions will be the only way to switch the steady profiles.

Unlike in budding yeast cells [11], there is no experimental evidence that *C. elegans* cells can spontaneously polarize, which means that the system is truly bistable. Traditionally, it has been speculated that the bistability comes from mutual inhibition of the aPAR and pPAR proteins [6, 15]. But translating this idea into equations becomes much harder than might be expected! Indeed, ODEs based on first-order mass action kinetics of aPAR-pPAR inhibition *do not* yield bistable dynamics under any choice of parameters [3]. Attempts to overcome this have used stoichiometric coefficients for the biochemical equations that guarantee bistability [4, 5] or included actomyosin flows designed to transport the aPARs [14]. Both of these approaches are grounded more in intuition than in biological evidence, as there is no reason to doubt mass action kinetics, and recent experiments have shown that both aPARs and pPARs are transported by myosin [7].

Recent experimental observations about PAR-3 provide a potential way out of this conundrum. Indeed, it was recently shown that PAR-3 asymmetries are stable even in the absence of all posterior inhibitors, which suggest that the dynamics of PAR-3 *by itself* are intrinsically bistable [8]. Experimental evidence has shown that the bistability occurs via a mechanism in which membrane-bound PAR-3 recruits additional cytoplasmic monomers to the membrane. One goal of this section is to

1

translate these observations into equations which demonstrate how PAR-3 can set up and maintain an asymmetry in the absence of posterior inhibition. We then incorporate posterior PAR proteins and show how their inclusion modifies the dynamics of PAR-3, potentially shifting the boundary between the two protein domains.

1.1 Basic equations and framework for PAR-3

We first formulate our model of PAR-3 dynamics, which is based loosely on that of Lang and Munro [10]. The key property of PAR-3 that makes it different from other proteins is its ability to form *oligomers* on the membrane. Unlike monomers, these oligomers do not diffuse in the membrane, and are not found in high concentrations in the cytoplasm. Based on these experimental observations, we will consider a model in which there are two species of PAR-3,

1. Monomeric PAR-3, which can be found in cytoplasmic form (A_{cyto}) or membrane bound (A_1) form.

2. Oligomerized PAR-3 (A_n) which is only found on the membrane and can neither diffuse nor become unbound. These assumptions are approximations based on the experimental observations in [8, Fig. 3K], which show that the dissociation rate constant for dimers in trimers is 5–10 times smaller than that for monomers, and also the experimental observation that PAR-3 only binds to the membrane in monomer form [8].

Given these assumptions, the model equations in dimensional form are as follows

$$\partial_t A_1 = D_A \partial_x^2 A_1 + \left(k_A^{\text{on}} + k_A^+ f_A^+ \left(A_1 + 2A_n \right) \right) A_{\text{cyto}} + 2k_A^{\text{dp}} A_n - 2k_A^{\text{p}} A_1^2 - k_A^{\text{off}} A_1 \tag{1a}$$

$$\partial_t A_n = k_A^{\text{p}} A_1^2 - k_A^{\text{dp}} A_n \tag{1b}$$

$$A_{\text{cyto}} = \frac{1}{hL} \left(A^{(\text{Tot})} L - \int_0^L \left(A_1(x) + 2A_n(x) \right) \, dx \right) \tag{1c}$$

A complete list of parameters with units and values is given in Table 1, but it will be helpful to point out the important ones in our model. First, the feedback strength k_A^+, which has units of length/time, gives the rate at which cytoplasmic PAR-3 is recruited to the membrane. It is multiplied by the dimensionless flux function f_A^+, which gives the dimensionless strength of recruitment as a function of the total bound PAR-3. The overall on rate is proportional to the cytoplasmic concentration, which is defined in (1c). There $A^{(\text{Tot})}$ expresses the density of bound PAR-3 when all molecules are bound to the membrane (units 1/length). Subtracting the amount of bound PAR-3 and dividing by the membrane area gives the cytoplasmic concentration in units of 1/area.

1.1.1 Dimensionless form

A sensible timescale for the system is the time a given PAR-3 molecule spends on the membrane. Because about 80% of the bound PAR-3 molecules are in oligomer form, and since the depolymerization reaction is much slower than the unbinding reaction, we nondimensionalize time by $1/k_A^{\mathrm{dp}}$. This gives the dimensionless (hatted) variables defined by

$$x = \hat{x}L \qquad t = \hat{t}/k_A^{\mathrm{dp}} \qquad Y = \hat{Y}Y^{(\mathrm{Tot})}.$$

Substituting into (1) gives the rewritten dynamics

$$\partial_{\hat{t}}\hat{A}_1 = \hat{D}_A\partial_{\hat{x}}^2 A_1 + \hat{K}_A^{\mathrm{on}}\left(1 + \hat{K}_A^+ f_A^+\left(\hat{A}_1 + 2\hat{A}_n\right)\right)\left(1 - \int_0^1 \left(\hat{A}_1(x) + 2\hat{A}_n(x)\right)d\hat{x}\right)$$

$$+ 2\hat{K}_A^{\mathrm{dp}}\hat{A}_n - 2\hat{K}_A^{\mathrm{p}}\hat{A}_1^{\,2} - \hat{K}_A^{\mathrm{off}}\hat{A}_1 \tag{2a}$$

$$\partial_{\hat{t}}\hat{A}_n = \hat{K}_A^{\mathrm{p}}\hat{A}_1^{\,2} - \hat{K}_A^{\mathrm{dp}}\hat{A}_n \tag{2b}$$

$$\hat{D}_A = \frac{D_A}{L^2 k_A^{\mathrm{dp}}}, \quad \hat{K}_A^{\mathrm{on}} = \frac{k_A^{\mathrm{on}}}{k_A^{\mathrm{dp}}h}, \quad \hat{K}_A^+ = \frac{k_A^+}{k_A^{\mathrm{on}}}, \quad \hat{K}_A^{\mathrm{off}} = \frac{k_A^{\mathrm{off}}}{k_A^{\mathrm{dp}}}, \quad \hat{K}_A^{\mathrm{p}} = \frac{k_A^{\mathrm{p}}A^{(\mathrm{Tot})}}{k_A^{\mathrm{dp}}}, \quad \hat{K}_A^{\mathrm{dp}} = 1 \tag{2c}$$

1.1.2 Linear feedback model

We first look at the dynamics of PAR-3 with the linear feedback model

$$f_A^+(x) = x,$$

similar to what was used by Lang and Munro [10]. The uniform steady state for A_1 can be found by first solving (2b) at steady state to obtain

$$A_n = \frac{\hat{K}_A^{\mathrm{p}}}{\hat{K}_A^{\mathrm{dp}}}\hat{A}_1^{\,2}. \tag{3}$$

Substituting this into (2a), we get a quartic equation for A_1 at steady state

$$0 = \hat{K}_A^{\mathrm{on}}\left(1 + \hat{K}_A^+\left(\hat{A}_1 + 2\frac{\hat{K}_A^{\mathrm{p}}}{\hat{K}_A^{\mathrm{dp}}}\hat{A}_1^{\,2}\right)\right)\left(1 - \left(\hat{A}_1 + 2\frac{\hat{K}_A^{\mathrm{p}}}{\hat{K}_A^{\mathrm{dp}}}\hat{A}_1^{\,2}\right)\right) - \hat{K}_A^{\mathrm{off}}\hat{A}_1,$$

which is just a polynomial and can be solved numerically. This quartic equation is controlled by three parameters: $\hat{K}_A^{\mathrm{on}}/\hat{K}_A^{\mathrm{off}}$, $\hat{K}_A^{\mathrm{p}}/\hat{K}_A^{\mathrm{dp}}$, and $\hat{K}_A^+$. A simple scan of these three parameters on the range $[0.01, 100]$ shows that this equation has a single real root in the range $[0, 1]$. We denote the steady state as $\bar{\hat{A}}_1$ and $\bar{\hat{A}}_n$.

1.1.3 Linear stability analysis

We now need to determine if the uniform steady state is stable. To do this, we consider a perturbation $\delta\hat{A}_1$ and $\delta\hat{A}_n$ with $\int_0^1 \delta\hat{A}_1(x)\,dx = \int_0^1 \delta\hat{A}_n(x)\,dx = 0$. The resulting linearized equations for the kth Fourier mode of A_1 and A_n can be written as

$$\frac{d}{dt}\begin{pmatrix}\hat{A}_1^{(k)}\\[4pt]\hat{A}_n^{(k)}\end{pmatrix} = \begin{pmatrix}-\hat{K}_A^{\text{off}} + \bar{\bar{A}}_c\hat{K}_A^+\hat{K}_A^{\text{on}} - 4\bar{\bar{A}}_1\hat{K}_A^{\text{p}} - 4\pi^2 k^2\hat{D}_A & 2\left(\hat{K}_A^{\text{dp}} + \bar{\bar{A}}_c\hat{K}_A^+\hat{K}_A^{\text{on}}\right)\\[4pt] 2\bar{\bar{A}}_1\hat{K}_A^{\text{p}} & -\hat{K}_A^{\text{dp}}\end{pmatrix}\begin{pmatrix}\hat{A}_1^{(k)}\\[4pt]\hat{A}_n^{(k)}\end{pmatrix}$$

$$\bar{\bar{A}}_c = 1 - \bar{\bar{A}}_1 - 2\bar{\bar{A}}_n$$

As such, the uniform steady state is unstable when the determinant of this matrix (with $k = 1$)

$$\hat{K}_A^{\text{dp}}(\hat{K}_A^{\text{off}} + 4\pi^2\hat{D}_A) - \bar{\bar{A}}_1\hat{K}_A^{\text{dp}}\hat{K}_A^+\hat{K}_A^{\text{on}} - 4\bar{\bar{A}}_1\bar{\bar{A}}_c\hat{K}_A^+\hat{K}_A^{\text{on}}\hat{K}_A^{\text{p}} < 0$$

$$\hat{K}_A^+\hat{K}_A^{\text{on}}\left(\bar{\bar{A}}_1\hat{K}_A^{\text{dp}} + 4\bar{\bar{A}}_1\bar{\bar{A}}_c\hat{K}_A^{\text{p}}\right) > \hat{K}_A^{\text{dp}}(\hat{K}_A^{\text{off}} + 4\pi^2\hat{D}_A) \tag{4}$$

Although this equation is somewhat misleading because $\bar{\bar{A}}_1$ is a function of the other parameters, it gives us the following observations, some of which are immediate, and some of which we determined numerically:

1. The uniform steady state can always be made stable by making the diffusion sufficiently fast.

2. Conversely, the uniform steady state can be made unstable by increasing the feedback $\hat{K}_A^+$.

3. In contrast to how it appears in (4), it turns out that the steady state is stable for *higher* values of $\hat{K}_A^{\text{on}}$, because of cytoplasmic depletion. Specifically, if there is so much protein bound at the uniform steady state, there will not be any more to be recruited to destabilize it. So the uniform steady state is actually unstable when $\hat{K}_A^{\text{on}}$ is sufficiently *small* so as to leave enough cytoplasmic protein. As such, this parameter is not really that interesting to study going forward.

4. For a fixed amount of membrane-bound protein, having more in the oligomerized state (either by increasing $\hat{K}_A^{\text{p}}$ or decreasing $\hat{K}_A^{\text{dp}}$) assists in making the uniform state unstable because oligomers can't diffuse and thus diffusion is effectively slower.

1.1.4 Parameters

To effectively constrain the model, we need values for at least some of the parameters. Table 1 provides a start to this by listing the parameters which are known definitively from experimental

Parameter	Description	Value	Units	Ref	Notes
L	Domain length	67.33	μm	[4]	$27 \times 15\ \mu$m ellipse
h	Cytoplasmic thickness	4.7	μm	[4]	(area/circumference)
D_A	Monomeric PAR-3 diffusivity	0.1	μm^2/s	[8]	
D_P	PAR-2 diffusivity	0.15	μm^2/s	[5]	
k_A^{on}	Monomeric PAR-3 attachment rate	1	μm/s		20% attached no feedback [8, Fig. 2]
k_P^{on}	Monomeric PAR-2 attachment rate	0.13	μm/s	[5]	
k_A^{off}	Monomeric PAR-3 detachment rate	3	1/s	[8]	(Fig. 3K)
k_P^{off}	PAR-2 detachment rate	7.3×10^{-3}	1/s	[5]	
k_A^{+}	PAR-3 self recruitment rate	?	μm/s		Control knob for PAR-3
k_A^{p}	PAR-3 polymerization rate	0.03	μm/s		30% monomers no feedback [8, Fig. 3G]
k_A^{dp}	PAR-3 depolymerization rate	0.08	1/s	[8]	Fig. 4E therein
r_{AP}	Rate of PAR-2 inhibition by PAR-3		μm/s		
r_{PA}	Rate of PAR-3 inhibition by PAR-2		μm/s		
$A^{(\mathrm{Tot})}$	Maximum bound PAR-3 density	50	#/μm	[4]	171 nM cytoplasmic (PAR-6)
$P^{(\mathrm{Tot})}$	Maximum bound PAR-2 density	50	#/μm		Same as PAR-6

Table 1: Parameter values for PAR-3 and PAR-2 model.

observations. It leaves three parameters which are not directly known: the on rate k_A^{on}, the polymerization rate k_A^{p}, and the feedback strength k_A^{+}. This is of course in addition to the feedback function f_A^{+}, which we here assume to be linear.

To obtain parameters which are unknown, we will first assume that the feedback is small, and fit the observations to the posterior side of wild-type embryos. If we assume that the total PAR-3 concentration is roughly maximum in the anterior half, then the posterior side will have $\hat{A}_1 + 2\hat{A}_n = 0.2$ [8, Fig. 2], and roughly 30% of the PAR-3 is in oligomer form [8] (this comes from $\alpha = 0.42$ as the exponenon for the exponential distribution on the posterior side). We then look for values of k_A^{on} and k_A^{p} that give these values, finding $k_A^{\mathrm{on}} = 1\ \mu$m/s and $k_A^{\mathrm{p}} = 0.03\ \mu$m/s. These leaves us k_A^{+} as a control knob for the dynamics.

To obtain $A^{(\mathrm{Tot})}$, we work off the observations in [4], where authors report 171 nM cytoplasmic concentration of PAR-6 if all molecules are cytoplasmic (we will assume PAR-3 is the same). Since $A_6^{(\mathrm{Tot})}$ is the maximum number density of PAR-6 when all are bound to the membrane, the conversion is

$$\left(\frac{171\ \mathrm{mol}}{\mathrm{L}}\right) \left(\frac{1\ \mathrm{L}}{10^{-15}\ \mu\mathrm{m3}}\right) \left(\frac{6.022 \times 10^{23}\mathrm{molecules}}{\mathrm{mol}}\right) \left(\frac{3180.86\ \mu\mathrm{m}^3}{\mathrm{embryo}}\right) \left(\frac{1\ \mathrm{embryo}}{67.33\ \mu\mathrm{m}}\right) \approx 50\ \frac{\mathrm{molecules}}{\mu\mathrm{m}}.$$

Here we are assuming the embryo in three dimensions is a $27 \times 15 \times 15$ ellipsoid [4], and using formulas for the circumference/area/volume for this shape.

1.1.5 Results

With these parameters set, the dimensionless parameters in (2c) are given as

$$\hat{D}_A = 2.8 \times 10^{-4}, \quad \hat{K}_A^{\mathrm{on}} = 2.7, \quad \hat{K}_A^+ = \frac{k_A^+}{k_A^{\mathrm{on}}}, \quad \hat{K}_A^{\mathrm{off}} = 37.5, \quad \hat{K}_A^{\mathrm{p}} = 18.8, \quad \hat{K}_A^{\mathrm{dp}} = 1$$

and so the parameter $\hat{K}_A^+$ provides a control knob by which we can study the system.

We begin our study by looking at the stability of the uniform state. In Fig. 1 (top plot), we examine the steady states and their stability as a function of the feedback parameter K_A^+. As the feedback increases, more oligomers are found in steady state. The limit to this is when there are about 75% oligomers, at which point the steady state becomes unstable. The bottom plot shows a further analysis of the stability. When the feedback is small enough ($\hat{K}_A^+ = 2$), perturbations around the steady state tend to drive the dynamics back to it, while for larger feedback ($\hat{K}_A^+ = 4$) perturbations are amplified. We note that what has to be considered for the stability analysis is *not* the absolute attachment rate (dotted blue), but the attachment rate *with the steady state cytoplasmic concentration.* This is because perturbations do not affect the cytoplasmic concentration (or do so only weakly).

What do the dynamics look like when we perturb around the steady state for different feedback strengths? In Fig. 2, we plot the dynamics using different colored lines with the same initial condition and two different choices of the feedback strength: $\hat{K}_A^+ = 2$ (which is expected to be stable) and $\hat{K}_A^+ = 4$ (unstable). We plot time in units of k_A^{dp}, so $\hat{t} = 1$ corresponds to 12.5 seconds of real time (thus $\hat{t} = 30$ corresponds to 10 minutes). We observe stable dynamics when $\hat{K}_A^+ = 2$ as expected, as the initially perturbed profile decays down to the uniform steady state. When $\hat{K}_A^+ = 4$, however, the dynamics are extreme, as the steady state is a very narrow peak which is limited by diffusion and depletion of the cytoplasmic pool. Since most of the monomers are in oligomer form, diffusion is almost zero, which makes the peak grow until the cytoplasmic pool is depleted.

We note that the growth of the peak is a point of disagreement between this work and that of Lang and Munro [10]. In that study, it was argued that the shift in the boundary is relatively slow, on the order of a hundred seconds per micron. So how can we explain the observations in Fig. 2, which show a more rapid shift in the boundary? The answer lies in the amount of available cytoplasmic protein. Our experiments are based on perturbations from *steady state*, where some
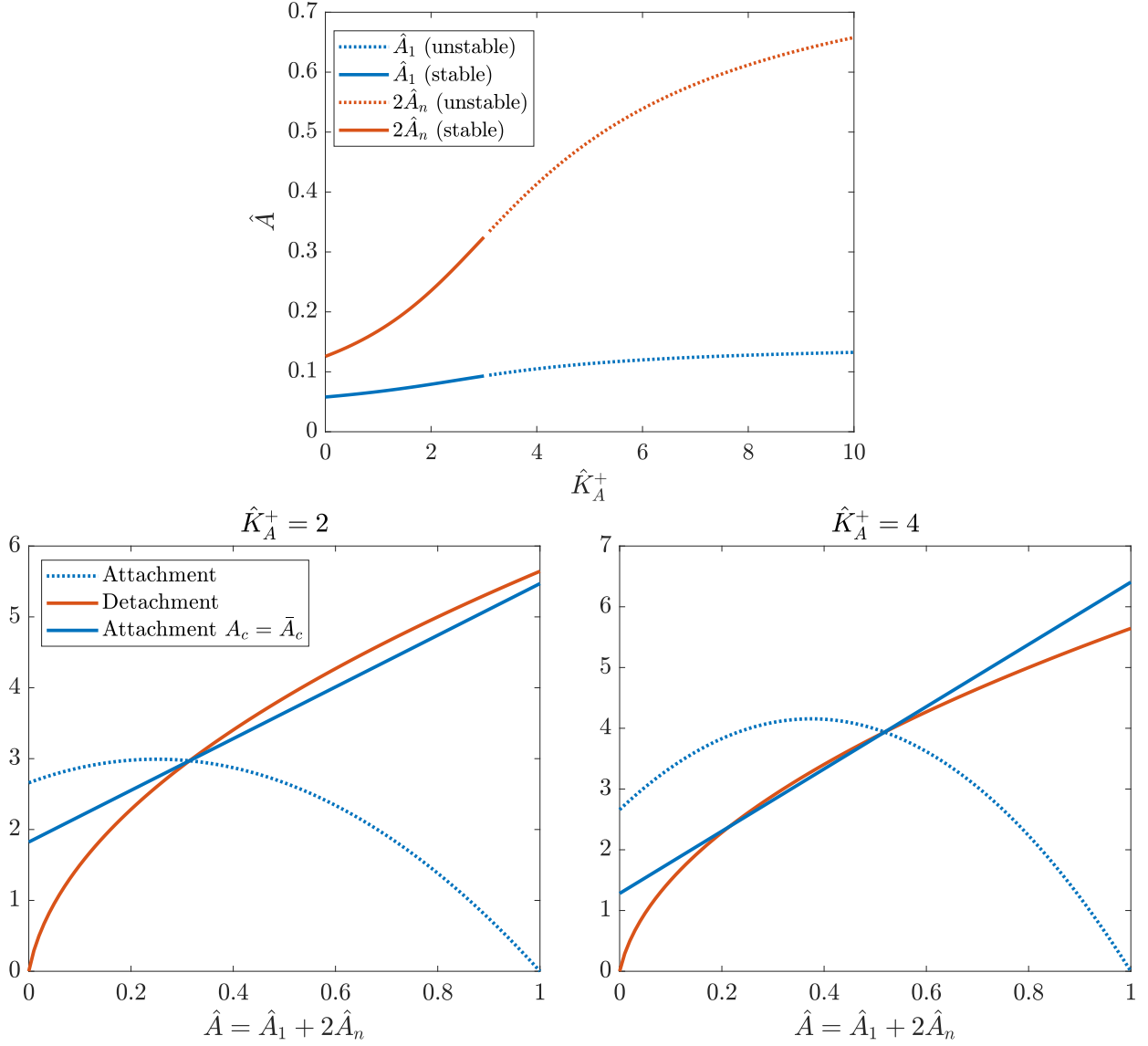
Figure 1: Steady states for the PAR-3 model **with linear feedback** as a function of dimensionless feedback strength. (Top:) The steady state bound monomer and oligomer proportion as a function of the feedback strength K_f^+. The blue line is the concentration of monomeric PAR-3, while the red is the concentration of oligomers. The solid lines represent stable steady states, while the dotted lines are unstable ones. (Bottom:) Flux plane analysis for the stable (left) and unstable (right) case. The stability analysis is determined by how the attachment rate (solid blue line, with constant cytoplasmic concentration) compares to the detachment rate (red) near the steady state.
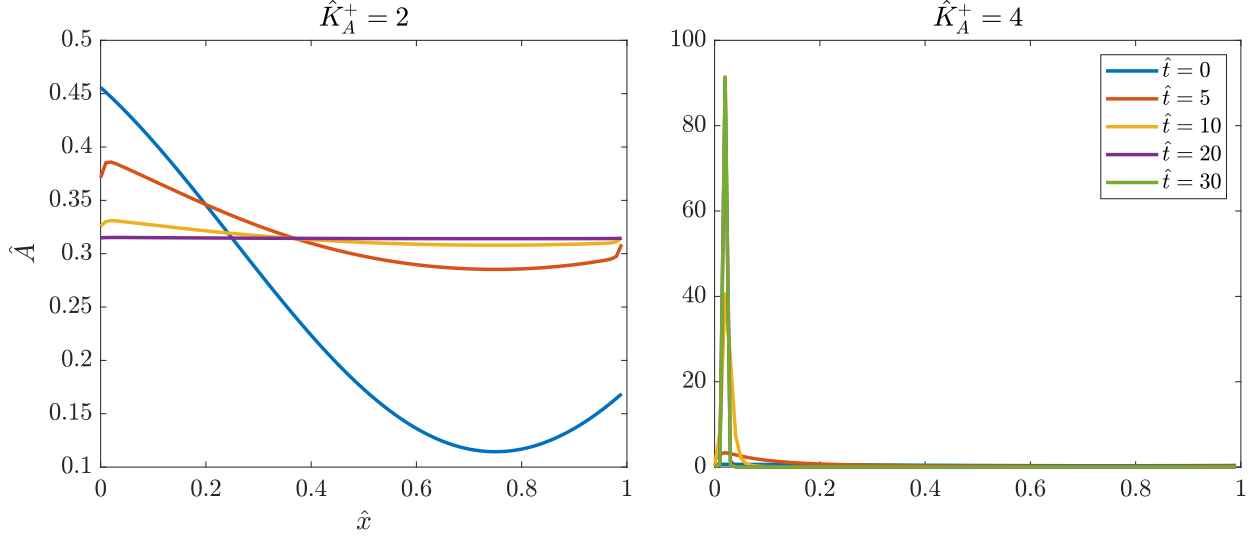
Figure 2: Dynamics of the PAR-3 model with linear feedback. We plot the dynamics using the same initial condition and two different choices of the feedback strength: $K_A^+ = 2$ (left) and $K_A^+ = 4$ (right). We plot time in units of k_A^{dp}, so $\hat{t} = 1$ corresponds to 12.5 seconds of real time (thus $\hat{t} = 30$ corresponds to about 10 minutes).

40% of the PAR-3 is bound and 60% is available in the cytoplasm. But the numerical experiments in [10, Fig. 4D] begin with a state where all of the protein is bound at time zero, which prevents the feedback from kicking in as rapidly, and gives a slower movement of the boundary.

No matter the initial condition, it is clear that the linear feedback model with large enough feedback strength develops a polarized state spontaneously, and in this case the region that contains more PAR-3 always outcompetes the region that contains less. This results in pulse-like shocks which don't slow down until the cytoplasmic pool is depleted. This contradicts the main experimental observation we want to explain, which is that PAR-3 can be stably enriched in half of the cortex, without contractility and without posterior PARs. The main reason for the contradiction is the feedback model: because we assume feedback proportional to monomer concentration, the feedback can only increase once the state is unstable. In the next section, we experiment with a nonlinear feedback model which gives results closer to the experiments.

1.2 PAR-3 model with feedback fit to experimental results

In the previous section, we saw that a linear feedback model for PAR-3 cannot explain the experimental data that shows stable enrichment of PAR-3 on one side of the cortex. The reason for this is that there is no cap to the feedback, and so it continues to concentrate protein until the

cytoplasmic pool is depleted.

There are really three key experimental observations that give us a hint as to the stability portrait of the PAR-3 dynamics:

1. The spatially uniform state is stable (for at least 10 minutes) in the absence of contractility.

2. The polarized state is stable once set up, even without contractility. That is, *at constant cytoplasmic concentration there are two stable steady states.*

3. Let u be the concentration of the uniform state. Then, at the polarized state, the concentration at the anterior end is $1.25u$ and $0.125u$ at the posterior end.

The key here is observation 2, which gives us important information about the flux plane. In particular, it tells us that the attachment rate has to equal the detachment rate (at constant cytoplasmic concentration) *three times*, with two giving stable steady states (and necessarily a middle one giving an unstable steady state). Since the detachment rate in this model is fixed, this observation essentially tells us what the feedback function should look like.

Let's see if a feedback function with a cap can match these observations. Specifically, we suppose that

$$f_A^+(x) = \min\left(x, f_{\max}\right),$$

which should limit the growth of unstable boundaries. Figure 3provides an example of how this might work, where we set the feedback $\hat{K}_A^+ = 8$ so that the steady state sits near $\hat{A} = 0.8$, and $f_{\max} = 1$. The uniform steady state is unstable (because the attachment flux exceeds the detachment flux near it), but the cap on the feedback makes the instability self-limiting, so that advances in the concentration will stall near $\hat{A} = 1.3$ (solid blue line meets solid red line). Unfortunately, because the feedback cap sits at 1, the uniform steady state will always be unstable. Because the uniform state is limited by 1, the attachment will always grow linearly there, which exceeds the rate of growth of detachment.

To remedy this problem, we need *the feedback to be saturated at the uniform steady state.* To do this, we adjust the parameters slightly so that $f_{\max} = 0.7$. To get a uniform steady state around $\hat{A} = 0.8$, we set $\hat{K}_A^+ = 12.5$. The resulting flux plane is shown in Fig. 4. There we see a *stable* steady state with $\hat{A} = 0.8$, and this is the only uniform steady state (dotted blue line and solid red line meet exactly once). The purple line shows what happens when we adjust the cytoplasmic concentration upwards to $\hat{A}_c = 0.25$; in this case there emerge two steady states, one with $\hat{A} \approx 1.25$

9
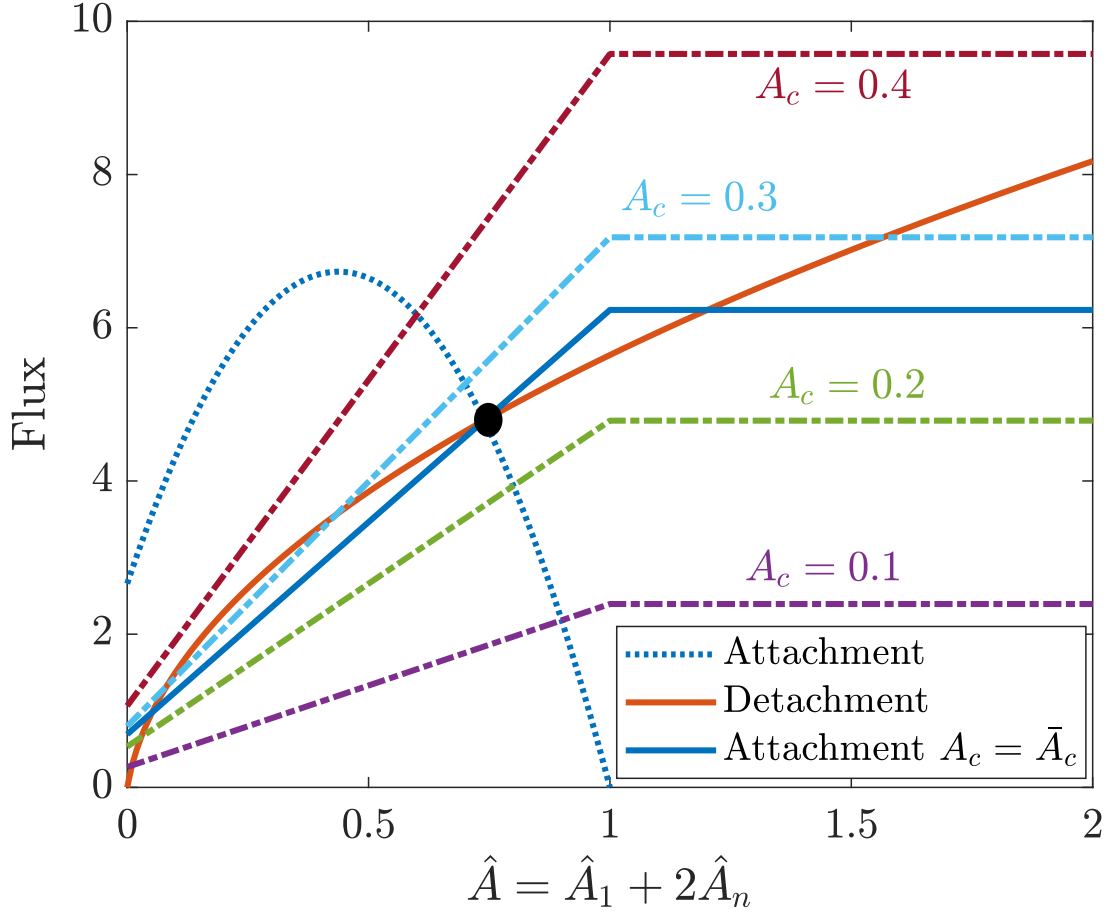
Figure 3: Flux plane with $f_{\max} = 1$ and $\hat{K}_A+ = 8$. We plot the attachment flux (assuming uniform concentration) as dotted blue, the detachment flux as solid red, and the attachment flux at the steady state cytoplasmic concentrated in solid blue. The dashed-dotted lines show different values of the cytoplasmic concentration. The black dot shows the uniform steady state.
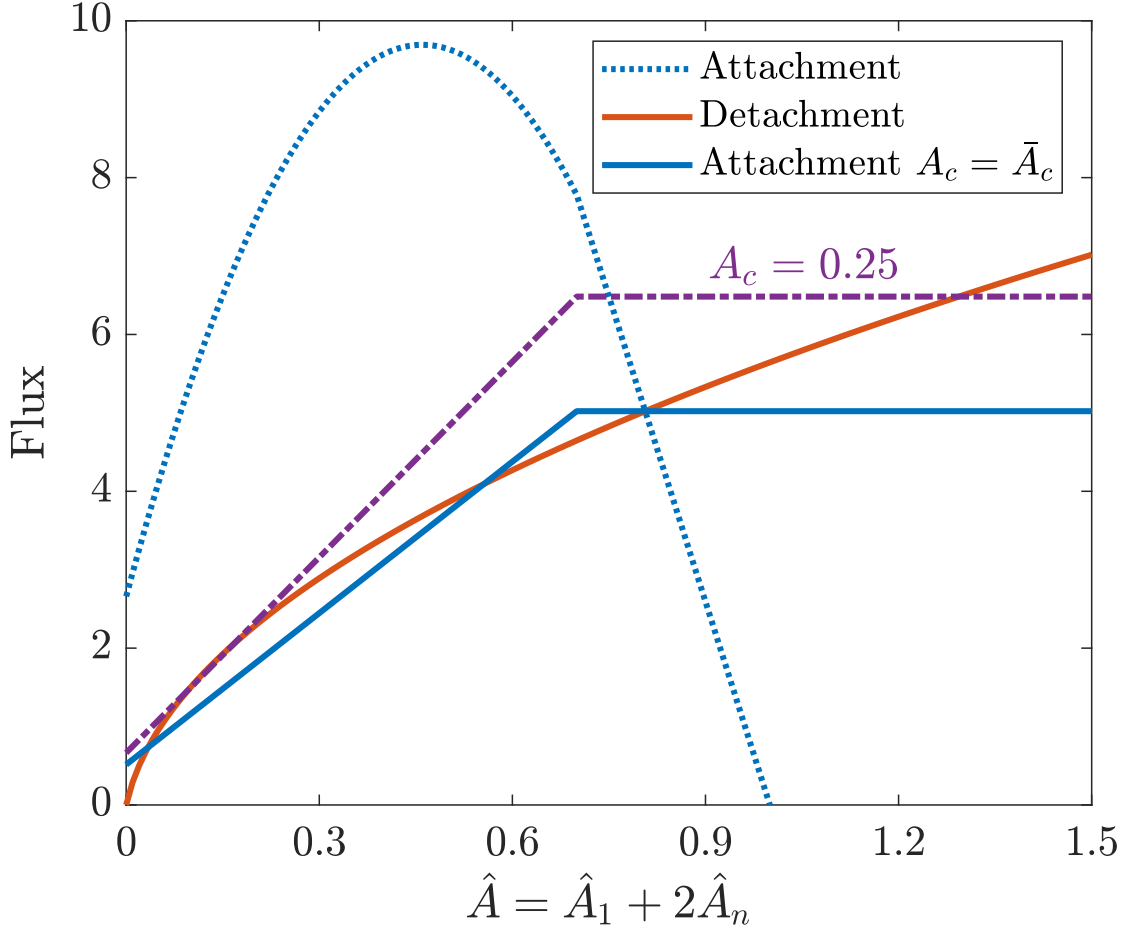
Figure 4: Flux plane with $f_{\max} = 0.7$ and $\hat{K}_A+ = 12.5$. We plot the attachment flux (assuming uniform concentration) as dotted blue, the detachment flux as solid red, and the attachment flux at the steady state cytoplasmic concentrated in solid blue. The dashed-dotted lines show different values of the cytoplasmic concentration. The black dot shows the uniform steady state.

and one with $\hat{A} \approx 0.1$. These new steady states are a consequence of the increased cytoplasmic concentration.

1.2.1 Results

Let's now see how the model performs when we fix $\hat{K}_A^+ = 12.5$ and $f_{\max} = 0.7$, so that the stability portrait is as shown in Fig. 5. In Figure 5, we show initial and final distributions of PAR-3. In the first row, we see that the uniform steady state is stable, as expected from the stability diagram. By contrast, when we introduce an asymmetry into the system by depleting PAR-3 in part of the domain, we see bistable dynamics where the small part gravitates to one steady state, while
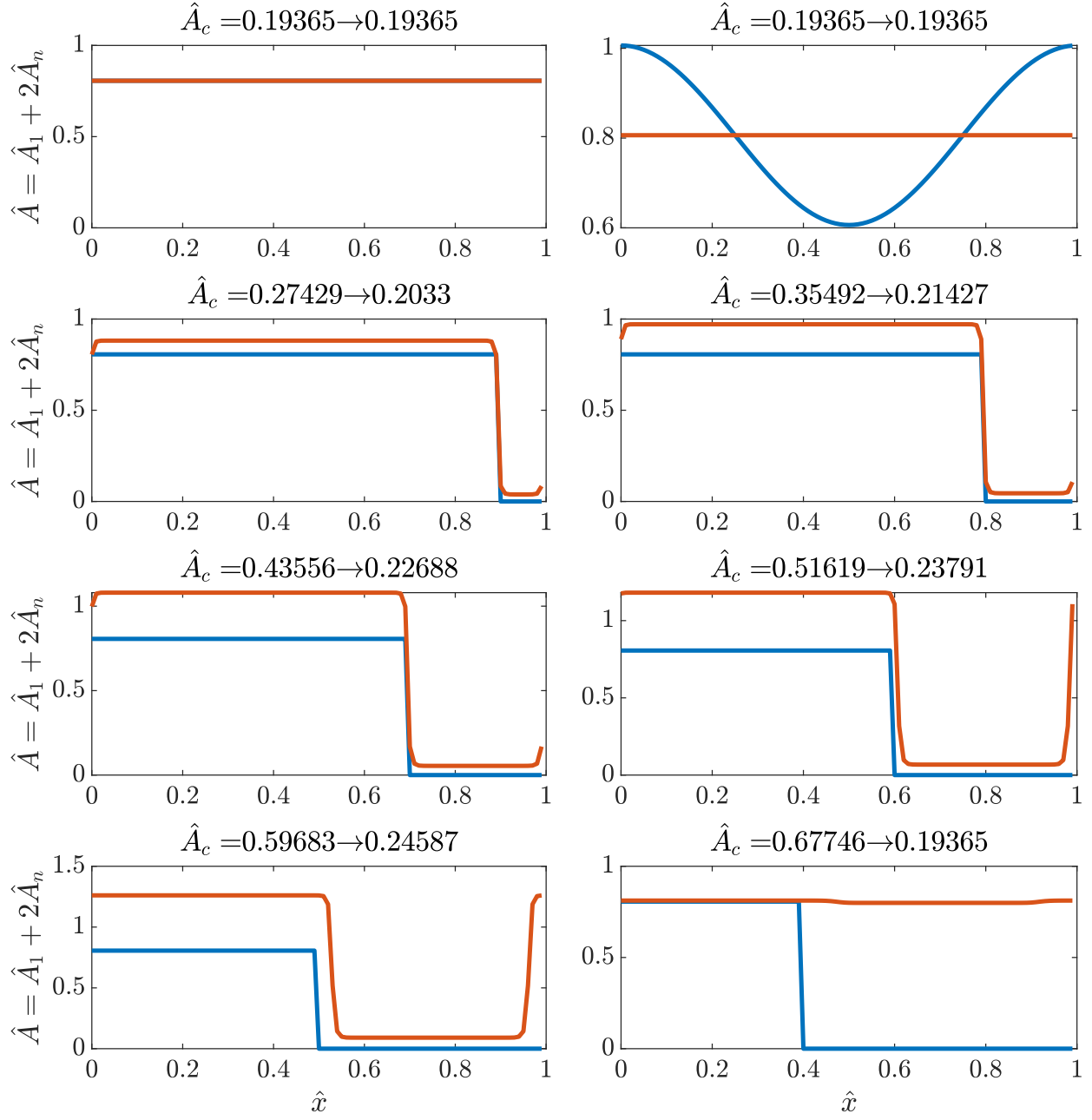
Figure 5: Simulating the PAR-3 feedback model with $\hat{K}_A^+ = 12.5$ and $f_{\max} = 0.7$. The initial states are shown in blue, and the final states are shown in red. The system can maintain an asymmetry for cytoplasmic concentration in a range near the uniform state.

the larger end goes to another. This bistability, however, only happens when the cytoplasmic concentration is in a range between 0.19 and 0.25. In the last panel at bottom right, the pattern would suggest a cytoplasmic concentration above 0.25, for which (see flux plane in Fig. 4) there is no smaller stable state (corresponding to the posterior half).

1.3   PAR-3 / PAR-2 bistable model

Let's now add posterior PARs (PAR-2) to the model of PAR-3, so that the equations are

$$\partial_t A_1 = D_A \partial_x^2 A_1 + \left(k_A^{\mathrm{on}} + k_A^+ f_A^+ \left(A_1 + 2A_n\right)\right) A_{\mathrm{cyto}} - k_A^{\mathrm{off}} A_1 - 2k_A^{\mathrm{p}} A_1^2 + 2k_A^{\mathrm{dp}} A_n, \tag{5a}$$

$$\partial_t A_n = k_A^{\mathrm{p}} A_1^2 - k_A^{\mathrm{dp}} A_n - r_{\mathrm{PA}} A_n \left(P_1 + P_2\right) \tag{5b}$$

$$\partial_t P = D_P \partial_x^2 P + k_P^{\mathrm{on}} P_{\mathrm{cyto}} - k_P^{\mathrm{off}} P - r_{\mathrm{AP}} P \left(A_1 + 2A_n\right), \tag{5c}$$

Here we have assumed that PAR-3 inhibits PAR-2 (by activating PKC-3, which is not included here for simplicity) [9]. It is possible here to model PAR-2 in terms of both dimers and monomers [1]; however, because PKC-3 acts on both monomers and dimers, the two are really only separated by kinetics of dimerization. Furthermore, a single species model of PAR-2 has already been made in [5], and the parameters for such a model were already fit there. As such, we will use a single species model for PAR-2.

Repeating our non-dimensionalization from (2), the dimensionless form of the equations (5) is

$$\partial_{\hat{t}} \hat{A}_1 = \hat{D}_A \partial_{\hat{x}}^2 A_1 + \hat{K}_A^{\mathrm{on}} \left(1 + \hat{K}_A^+ f_A^+ \left(\hat{A}_1 + 2\hat{A}_n\right)\right) \left(1 - \int_0^1 \left(\hat{A}_1(x) + 2\hat{A}_n(x)\right) d\hat{x}\right)$$
$$+ 2\hat{K}_A^{\mathrm{dp}} \hat{A}_n - 2\hat{K}_A^{\mathrm{p}} \hat{A}_1^2 - \hat{K}_A^{\mathrm{off}} \hat{A}_1 \tag{6a}$$

$$\partial_{\hat{t}} \hat{A}_n = \hat{K}_A^{\mathrm{p}} \hat{A}_1^2 - \hat{K}_A^{\mathrm{dp}} \hat{A}_n - \frac{r_{\mathrm{PA}} P^{(\mathrm{Tot})}}{k_A^{\mathrm{dp}}} \hat{P} \hat{A}_n \tag{6b}$$

$$\partial_{\hat{t}} \hat{P} = \hat{D}_P \partial_{\hat{x}}^2 \hat{P} + \hat{K}_P^{\mathrm{on}} \left(1 - \int_0^1 \hat{P}(\hat{x}) d\hat{x}\right) - \hat{K}_P^{\mathrm{off}} \hat{P} - \frac{r_{\mathrm{AP}} A^{(\mathrm{Tot})}}{k_A^{\mathrm{dp}}} \left(\hat{A}_1 + 2\hat{A}_n\right) \hat{P} \tag{6c}$$

$$\hat{D}_A = \frac{D_A}{L^2 k_A^{\mathrm{dp}}}, \quad \hat{K}_A^{\mathrm{on}} = \frac{k_A^{\mathrm{on}}}{k_A^{\mathrm{dp}} h}, \quad \hat{K}_A^+ = \frac{k_A^+}{k_A^{\mathrm{on}}}, \quad \hat{K}_A^{\mathrm{off}} = \frac{k_A^{\mathrm{off}}}{k_A^{\mathrm{dp}}}, \quad \hat{K}_A^{\mathrm{p}} = \frac{k_A^{\mathrm{p}} A^{(\mathrm{Tot})}}{k_A^{\mathrm{dp}}}, \quad \hat{K}_A^{\mathrm{dp}} = 1 \tag{6d}$$

$$\hat{D}_P = \frac{D_P}{L^2 k_A^{\mathrm{dp}}} \quad \hat{K}_P^{\mathrm{on}} = \frac{k_P^{\mathrm{on}}}{k_A^{\mathrm{dp}} h}, \quad \hat{K}_P^{\mathrm{off}} = \frac{k_P^{\mathrm{off}}}{k_A^{\mathrm{dp}}} \tag{6e}$$

Using the parameters in Table 1, there are three unknown parameters here: the feedback strength K_A^+, which we will fix at $K_A^+ = 12.5$ to obtain bistability of the intrinsic PAR-3 dynamics, and the inhibition parameters r_{AP} and r_{PA}. For simplicity, we will assume $r_{\mathrm{AP}} = r_{\mathrm{PA}}$.
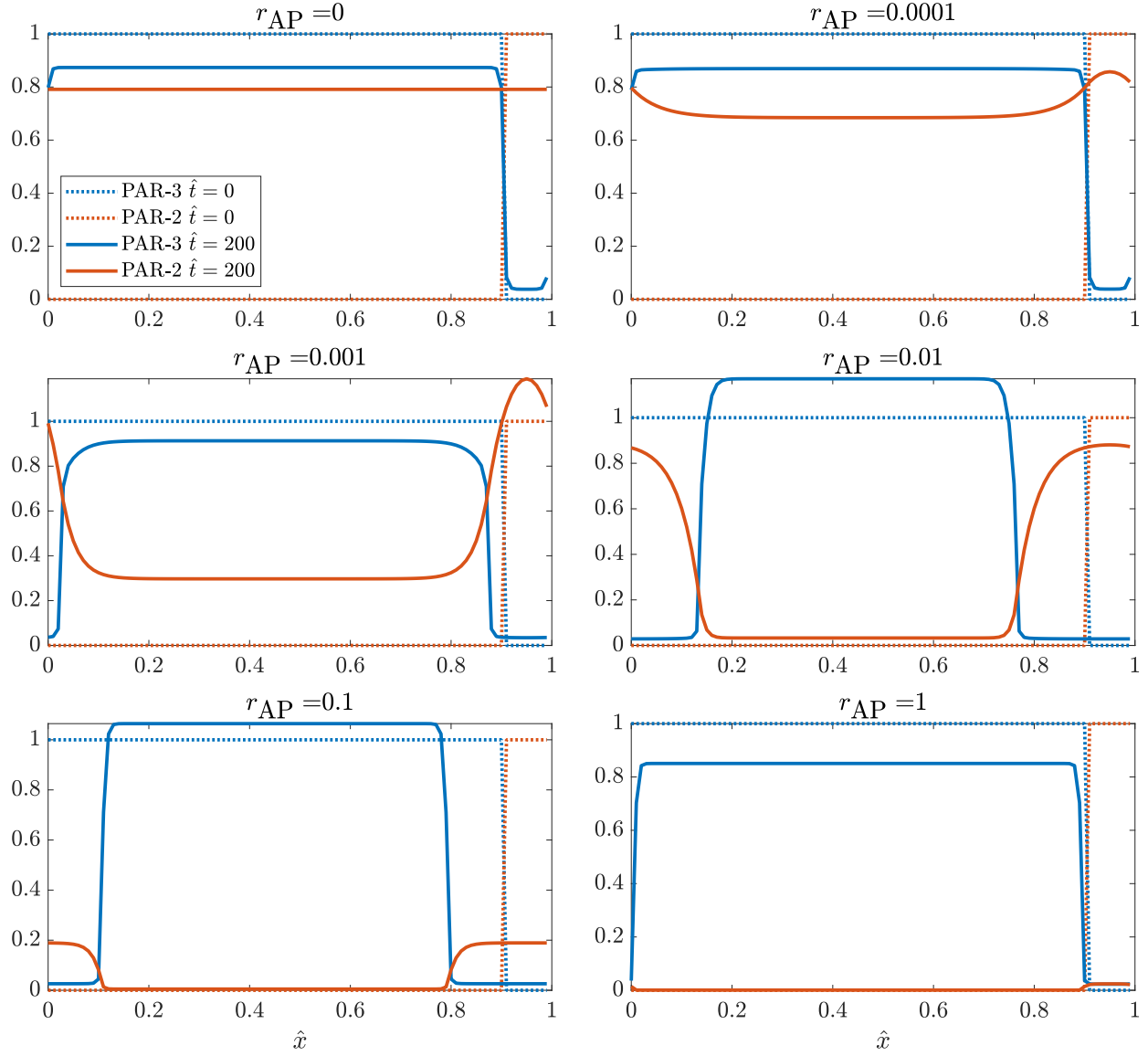
Figure 6: Dynamics of the PAR-2/PAR-3 model (6) with an initial small zone of PAR-2 enrichment and PAR-3 depletion. The dotted lines show the initial conditions, while the solid lines show the steady state, both for PAR-3 in blue and PAR-2 in red.

As an illustration of how this model behaves, in Fig. 7 we examine how an initially small zone of PAR-2 enrichment evolves to its steady state. The key here is the dynamics of PAR-3, which we recall switches between a small steady state (typically associated with the posterior half), and a larger steady state (typically associated with the anterior half). When there is no inhibition, PAR-3 develops its bistable state naturally, and PAR-2 is spread uniformly. Increasing the mutual inhibition then causes the boundary to shift, as depletion of PAR-2 in the interior leads to more cytoplasmic PAR-2, which increases the on rate in the inhibited zone. The attaching PAR-2 then diffuses, out-competing the PAR-3 and driving it to a lower steady state. This shifts the boundary. When mutual inhibition goes back up, PAR-2 simply can't do anything because the mutual inhibition is too strong. We note also the shape of peak in PAR-2 is more broad than for PAR-3, since we assume that PAR-2 can diffuse in the membrane with a higher diffusion coefficient than even monomeric PAR-3, and since PAR-3 is mostly in the non-diffusive oligomer form.

1.3.1 Effect of depleting one protein

Looking at the dimensionless system (6), there is a clear dependence of the reaction terms on the ratio of anterior/posterior proteins. For example, if $P^{(\text{Tot})} > A^{(\text{Tot})}$, then even if the mutual inhibition strength $r_{\text{AP}} = r_{\text{PA}}$, there will still be an imbalance in the reaction terms which could shift the direction of the boundary. We look at this in more detail in Fig. 8, where we show the steady states for different values of $A^{(\text{Tot})}$ and $P^{(\text{Tot})}$. Along each *row*, we fix the total amount of PAR-2, finding that when we deplete PAR-3 we see a significant expansion of the posterior PAR-2 domain. Likewise, along each *column*, we fix the total amount of PAR-3, finding that depleting PAR-2 will contract the posterior PAR-2 domain.

We should discuss what the experiments tell us about the PAR-3/PAR-2 circuit *without* contractility. What is this model missing, if anything?

2   Myosin and CDC-42

Now that we have set up a biochemical circuit that can maintain a stable polarized state in the absence of contractility, we turn to the incorporation of actomyosin flows. This section constitutes the meat of this project, as it explores how actomyosin *combines* with the PAR protein circuit to maintain polarity.
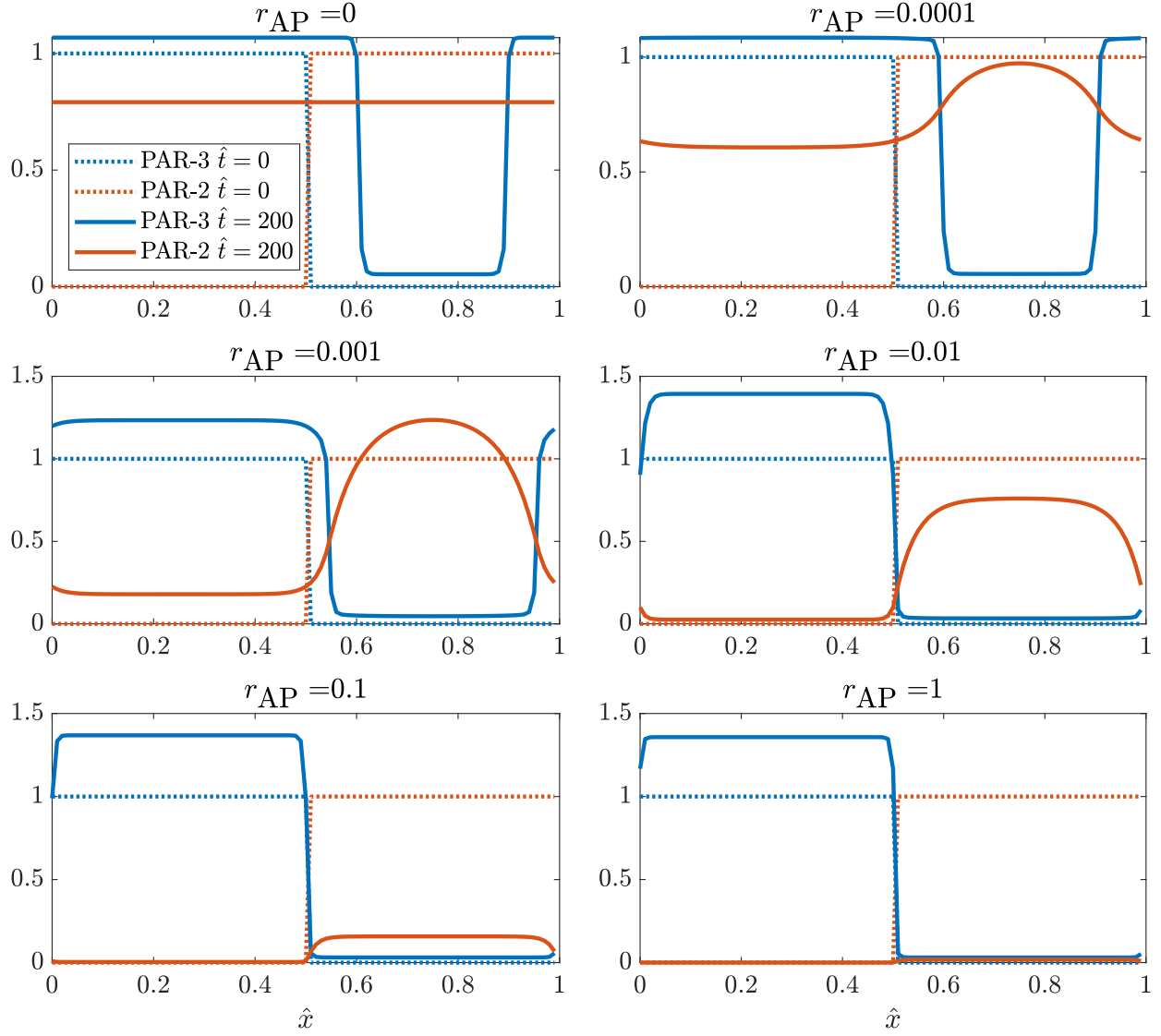
Figure 7: Dynamics of the PAR-2/PAR-3 model (6) with initially equal zones of PAR-2 and PAR-3 enrichment. The dotted lines show the initial conditions, while the solid lines show the steady state, both for PAR-3 in blue and PAR-2 in red.
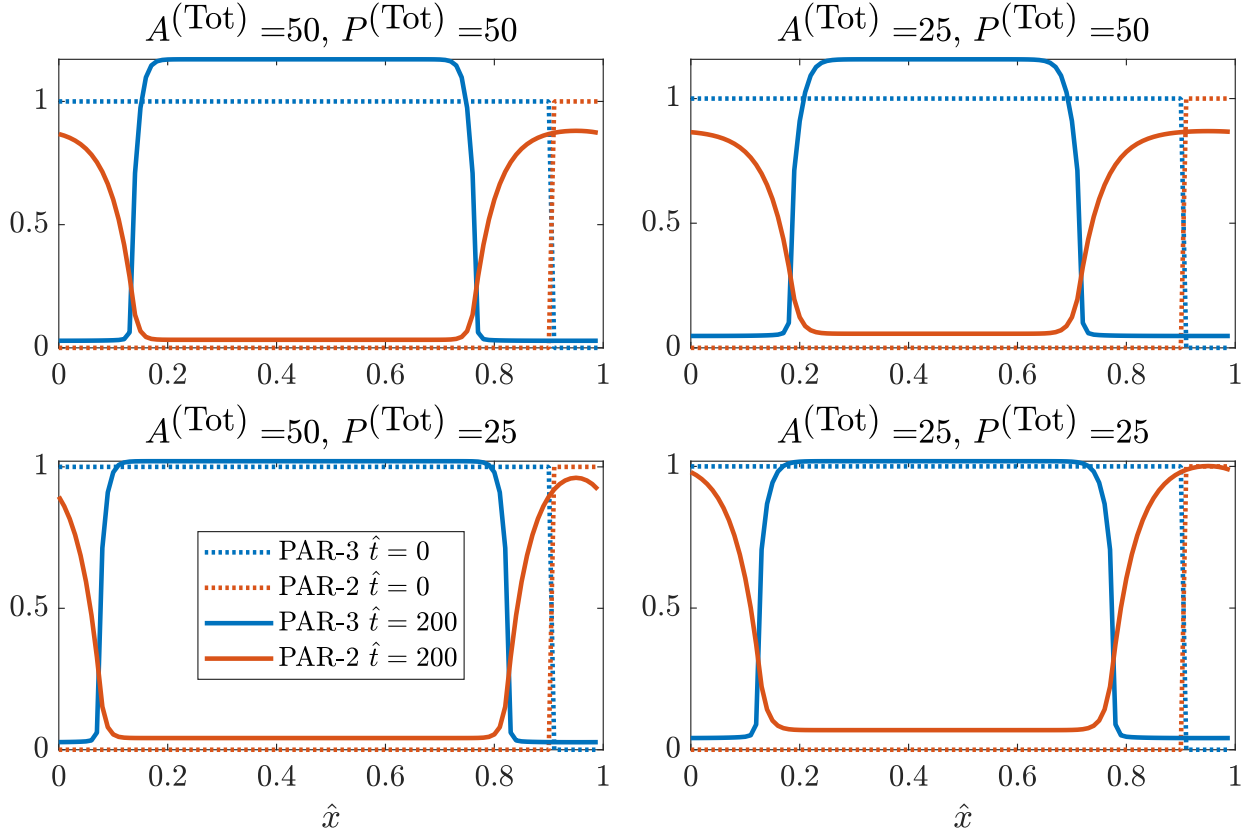
Figure 8: Dynamics of the PAR-2/PAR-3 model (6) with an initial small zone of PAR-2 enrichment and PAR-3 depletion. The dotted lines show the initial conditions, while the solid lines show the steady state, both for PAR-3 in blue and PAR-2 in red. Here we fix $r_{\mathrm{AP}} = 10^{-2}$ and vary the total amount of each protein.

2.1 Experimental observations

The goal of this section specifically is to explain the following experimental observations:

1. In wild-type embryos, myosin is stably enriched on the anterior side.

2. Without CDC-42, asymmetries in myosin are unstable, and there is a uniform distribution of myosin throughout the embryo.

3. Embryos depleted of arp 2/3 (branched actin) display a shrunken anterior domain with concentrated myosin activity.

4. In embryos where polarity establishment is blocked, myosin-based cortical flows can "rescue" asymmetries. The rescue process happens when small asymmetries in PAR protein concentrations are strongly amplified by myosin-based flows.

2.2 Myosin as a self-patterning material

Let us begin by building a toy model for myosin dynamics. This section is a summary of the paper [2], which considers the same problem. The novelty in what we do will come later, when we couple myosin to branched actin and other proteins.

We describe the dynamics of myosin $M(x,t)$ using the advection-diffusion equation

$$\partial_t M + \partial_x (vM) = D_M \partial_x^2 M. \tag{7}$$

The complication is that the myosin is advected through a velocity field of its own making. The velocity field comes from stress generated in the fluid,

$$\sigma = \eta \partial_x v + \sigma_a(M), \tag{8}$$

which is a combination of viscous stress and active stress. As in [2], we ignore the elastic part of the stress, assuming the actomyosin cortex is purely viscous when in reality it is visco-elastic. The force balance equation in the fluid says that the force due to stress must be balanced by the drag force,

$$\gamma v = \partial_x \sigma, \tag{9}$$

where γ is the drag coefficient. Combining the force balance (9) with the stress expression (8) gives an auxillary equation for the velocity field

$$\gamma v = \eta \partial_x^2 v + \partial_x \sigma_a(M) \tag{10}$$

18

which couples to the myosin equation (7) via the active stress.

The advection-diffusion equation (7) is mass-preserving, meaning that the uniform steady state is just given by $M_0 = \dfrac{1}{L} \displaystyle\int_0^L M(x,0)\, dx$. For the active stress, we let $\sigma_a = \sigma_0 a(M)$. The analysis of [2] shows that (for periodic boundary conditions) the uniform steady state is unstable when

$$\text{Pe} \times \frac{M_0\left(\partial_M a\left(M_0\right)\right)}{1 + \left(2\pi\ell/L\right)^2} > 1, \tag{11}$$

where $\ell = \sqrt{\eta/\gamma}$ is the characteristic lengthscale over which velocity decays (the diffusive lengthscale for velocity), L is the system length, and the Peclet number

$$\text{Pe} = \frac{\sigma_0}{D_M \gamma} \tag{12}$$

expresses the ratio of advective transport to diffusive transport. Qualitatively, the system has a uniform steady state and a second peaked steady state, where advective flux into the peaks matches the diffusive flux into the peaks. For this steady state to be stable, the advective transport must be sufficiently large relative to diffusive transport, so the Peclet number must be sufficiently large.

2.3 Myosin pattern formation with turnover

We now introduce a single species model of myosin with turnover,

$$\partial_t M + \partial_x\left(vM\right) = D_M \partial_x^2 M + k_M^{\text{on}} M_{\text{cyto}} - k_M^{\text{off}} M \tag{13a}$$

$$\gamma v = \eta \partial_x^2 v + \partial_x \sigma_a(M) \tag{13b}$$

$$\sigma_a(M) = \sigma_0 \frac{M}{M^{(\text{Tot})} + M} \tag{13c}$$

The form of the active stress here is simply chosen so that σ_0 provides the scaling, with the rest of the function being (roughly) on $[0, 1]$. It will be useful to nondimensionalize this equation, using the scalings

$$x = \hat{x}L \qquad t = \hat{t}/k_M^{\text{off}} \qquad Y = \hat{Y}Y^{(\text{Tot})} \qquad v = \hat{v}\frac{\sigma_0}{\sqrt{\eta\gamma}} \tag{14}$$

The resulting equations are

$$\partial_{\hat{t}}\hat{M} + \hat{\sigma}_0 \partial_{\hat{x}}\left(\hat{v}\hat{M}\right) = \hat{D}_M \partial_{\hat{x}}^2 \hat{M} + \hat{K}_M^{\text{on}}\left(1 - \int_0^1 \hat{M}(x)\, dx\right) - \hat{M} \tag{15a}$$

$$\hat{v} = \hat{\ell}^2 \partial_{\hat{x}}^2 v + \hat{\ell}\partial_{\hat{x}}\hat{\sigma}_a(\hat{M}) \tag{15b}$$

$$\hat{\sigma}_a = \frac{\hat{M}}{1 + \hat{M}} \tag{15c}$$

Parameter	Description	Value	Units	Ref	Notes
L	Domain length	67.33	μm	[4]	27×15 μm ellipse
h	Cytoplasmic thickness	4.7	μm	[4]	(area/circumference)
D_C	CDC-42 diffusivity	0.1	μm^2/s	[12]	
D_M	Myosin diffusivity	0.05	μm^2/s	[5]	
D_R	Branched actin diffusivity	0.1	μm^2/s		Same as myosin
k_C^{on}	CDC-42/PAR-6 attachment rate	0.02	μm/s	[5]	
k_M^{on}	Myosin attachment rate	0.2	μm/s	[5]	
k_R^{on}	Branched actin attachment rate	0.2	μm/s		Same as myosin
k_C^{off}	PAR-6/CDC-42 detachment rate	0.01	1/s	[12]	
k_M^{off}	Myosin detachment rate	0.12	1/s	[5]	
k_R^{off}	Branched actin detachment rate	0.12	1/s		Same as myosin
η	Cytoskeletal fluid viscosity	0.1	Pa·s		$100 \times$ water
γ	Myosin drag coefficient	10^{-3}	Pa·s/μm^2	[5]	$\ell = \sqrt{\eta/\gamma} = 10\,\mu$m
σ_0	Stress coefficient and form	1.1×10^{-3}	Pa		See Sec. 2.4.3
$\hat{\sigma}_a(\hat{M})$	Stress function of myosin	$\hat{M}$			See Sec. 2.4.3
k_M^{E}	Rate of CDC-42 myosin promotion	?	μm^2/s		
k_R^{E}	Rate of CDC-42 branched actin promotion	?	μm^2/s		
$C^{(\text{Tot})}$	Maximum bound CDC-42 density	50	#/μm	[4]	Same as PAR-6
$M^{(\text{Tot})}$	Maximum bound myosin density	50	#/μm	[4]	Same as PAR-6
$R^{(\text{Tot})}$	Maximum bound branched actin density	50	#/μm	[4]	Same as PAR-6

Table 2: Parameter values for myosin model.

and are controlled by the dimensionless parameters

$$\hat{\sigma}_0 = \left(\frac{\sigma_0/\sqrt{\eta\gamma}}{Lk_M^{\text{off}}}\right) \qquad \hat{D}_M = \frac{D_M}{k_M^{\text{off}}L^2} \qquad \hat{K}_M^{\text{on}} = \frac{k_M^{\text{on}}}{hk_M^{\text{off}}} \qquad \hat{\ell} = \frac{\sqrt{\eta/\gamma}}{L}. \tag{16}$$

Recalling that $1/k_M^{\text{off}}$ is the residence time, these dimensionless parameters can be understood in the following way:

1. $\hat{\sigma}_0$ is the fraction of the domain that active transport occurs on before a myosin molecule jumps off. To see this, note that residence time $\times$ the advective velocity $\sigma_0/\sqrt{\eta\gamma}$ is the amount of motion, which is normalized by the domain length.

2. $\hat{D}_M$ is the maximum fraction of the domain a molecule diffuses before it unbinds (in the extreme case when the gradient in the domain is $1/L$, the diffusive velocity is D_M/L).

3. $\hat{K}_M^{\text{on}}$ is the ratio of the binding rate to unbinding rate when all the molecules are cytoplasmic. The uniform steady state of the model is given by $\hat{M}_0 = \hat{K}_M^{\text{on}}/\left(1 + \hat{K}_M^{\text{on}}\right)$.

4. $\hat{\ell}$ is the ratio of the hydrodynamic lengthscale to the domain length.

2.3.1 Linear stability analysis

The uniform steady state is $\hat{M}_0 = \hat{K}_M^{\text{on}}/\left(1 + \hat{K}_M^{\text{on}}\right)$. We consider a perturbation around that state $M = \hat{M}_0 + \delta M$, where $\delta M = \delta M_0 e^{\lambda(k)\hat{t}+2\pi ik\hat{x}}$. Plugging this into (21c), we get the velocity [2, Eq. (11)]

$$\hat{v} = \frac{2\pi ik\hat{\ell}\hat{\sigma}_a'(M_0)}{1 + \left(2\pi k\hat{\ell}\right)^2}\delta M. \tag{17}$$

Substituting this velocity into (15a), and considering only the first order terms, we get the following equation for the eigenvalues

$$\lambda(k) = \frac{4\pi^2 k^2 \hat{\ell}\hat{M}_0\hat{\sigma}_0\sigma_a'(\hat{M}_0)}{1 + 4\pi^2 k^2\hat{\ell}^2} - \hat{D}_M 4\pi^2 k^2 - 1 \tag{18}$$

Using the parameters in Table 2, we have the following known values for the dimensionless groups

$$\hat{D}_M \leq 2 \times 10^{-4} \qquad \hat{K}_M^{\text{on}} \approx 0.35 \rightarrow \hat{M}_0 \approx 0.26 \rightarrow \sigma_a'(M_0) \approx 0.63 \qquad \hat{\ell} \approx 0.15 \tag{19}$$

The upper bound on the diffusivity is obtained by using the diffusion constant of a protein monomer from Table 1 (0.1 μm^2/s). This gives the dispersion relation shown in Fig. 9 for different values of $\hat{\sigma}_0$. We observe strong flow coupling required for instability; with $\hat{\sigma}_0 = 1$ (flow transports myosins around the entire circumference of the cell before they come off), we still do not see any instability.
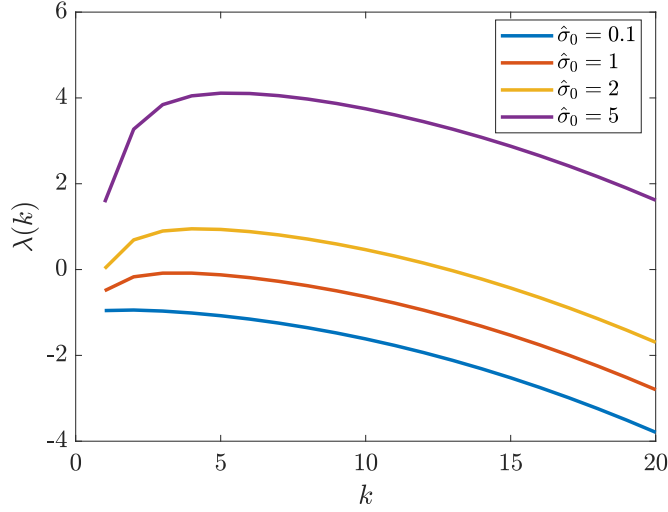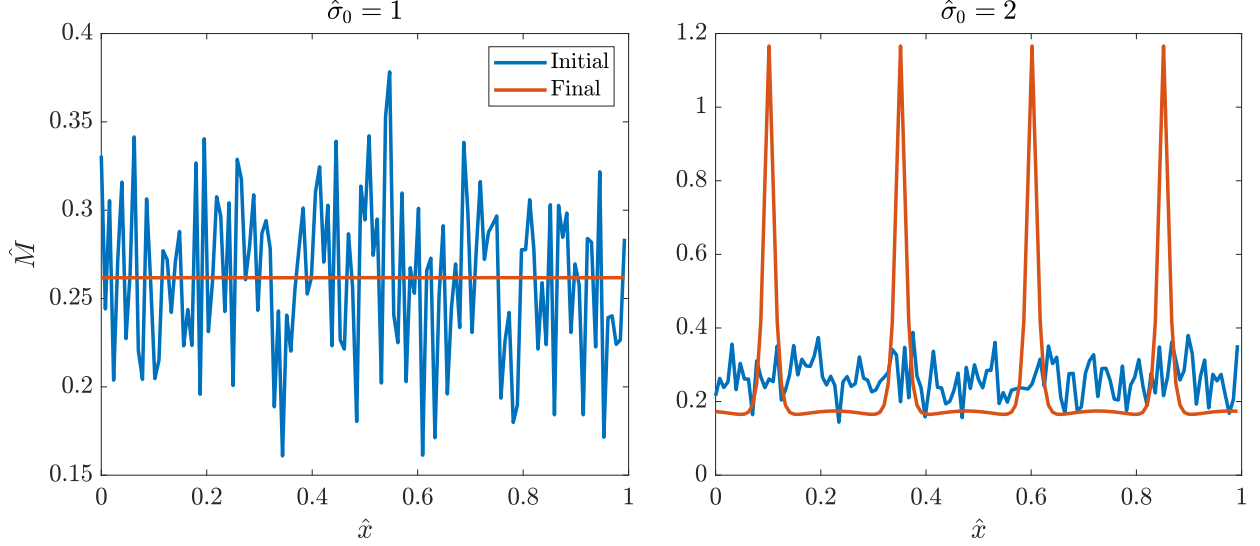
Figure 9: Dispersion relation (18) for myosin for different values of $\hat{\sigma}_0$. Positive eigenvalues indicate instability of the steady state.

Importantly, the -1 in the dispersion relation (18) comes from the unbinding kinetics; thus, unbinding, which happens proportional to the number of bound myosins, makes it *harder* to leave the steady state. Indeed, without the -1, the instability occurs at $\hat{\sigma}_0 \approx 0.02$, which is pretty weak coupling to the flow. When we account for unbinding, diffusion becomes so small as to be irrelevant, as for the $k = 1$ mode the coefficient in (18) is $\hat{D}_M 4\pi^2 \approx 0.007$. **Thus, the real balance here (to generate the instability) is not between advection and diffusion, but between advection and *unbinding*.** Specifically, the advective flow must be strong enough to overcome the increase in unbinding that happens in areas enriched in myosin.

So what do the steady states look like when the uniform steady state is unstable? Figure 10 shows that multiple peaks form when $\hat{\sigma}_0 = 2$. In this case, the advective flux into the peaks (flows have speeds 0.5 μm/s in dimensional units) balances diffusion and increased unbinding out of the peaks.

We note that the parameter $\hat{\sigma}_0 = 2$ required to generate the instability is extremely large. Indeed, Ed's 2012 manuscript measures the maximum cortical velocity at 9 μm/min$= 0.15\,\mu$m/s. The myosin residence time is roughly 10 s, so that is a transport of 1.5 μm while in residence. Divide by the domain length $L \approx 67\ \mu$m, and we get $\hat{\sigma}_0 \approx 0.022$, which demonstrates that 2 is an unreasonably large value. Thus, the model predicts that *myosin alone cannot spontaneously polarize*, which is in agreement with experimental observation 2 (see Section 2.1).

Figure 10: Myosin steady states for two different values of $\hat{\sigma}_0$ for myosin for different values of $\hat{\sigma}_0$. Positive eigenvalues indicate instability of the steady state.

2.4 Dynamics with CDC-42 recruiting myosin

We now consider a system where CDC-42 and myosin interact to generate patterns. The governing equations in dimensional form are

$$\partial_t C + \partial_x \left(vC \right) = D_C \partial_x^2 C + k_C^{\text{on}} C_{\text{cyto}} - k_C^{\text{off}} C \tag{20a}$$

$$\partial_t M + \partial_x \left(vM \right) = D_M \partial_x^2 M + \left(k_M^{\text{on}} + k_M^{\text{E}} C \right) M_{\text{cyto}} - k_M^{\text{off}} M \tag{20b}$$

$$\gamma v = \eta \partial_x^2 v + \partial_x \sigma_a(M) \tag{20c}$$

So that we have added an additional advection-diffusion equation for CDC-42, with its binding to the membrane promoting myosin.

In dimensionless form, these equations read

$$\partial_{\hat{t}} \hat{C} + \hat{\sigma}_0 \partial_{\hat{x}} \left(\hat{v}\hat{C} \right) = \left(\frac{D_C}{L^2 k_M^{\text{off}}} \right) \partial_{\hat{x}}^2 \hat{C} + \frac{k_C^{\text{on}}}{h k_M^{\text{off}}} \left(1 - \int_0^1 \hat{C}(x)\,dx \right) - \frac{k_C^{\text{off}}}{k_M^{\text{off}}} \hat{C} \tag{21a}$$
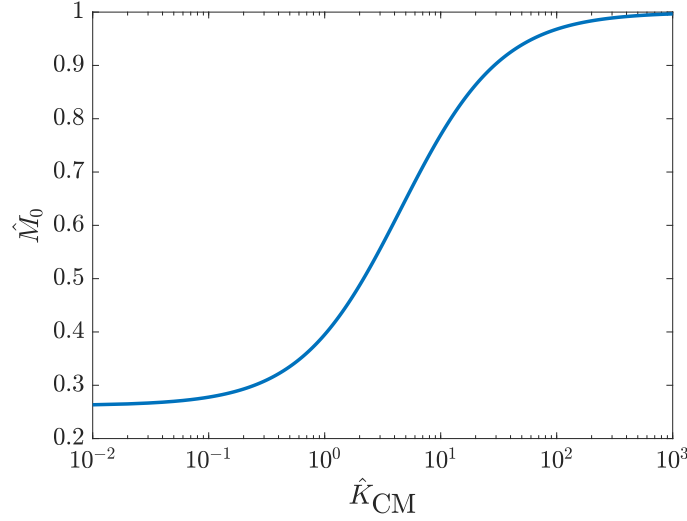
$$\partial_{\hat{t}} \hat{M} + \hat{\sigma}_0 \partial_{\hat{x}} \left(\hat{v}\hat{M} \right) = \hat{D}_M \partial_{\hat{x}}^2 \hat{M} + \left(\hat{K}_M^{\text{on}} + \hat{K}_{\text{CM}}\hat{C} \right) \left(1 - \int_0^1 \hat{M}(x)\,dx \right) - \hat{M} \tag{21b}$$

$$\hat{v} = \hat{\ell}^2 \partial_{\hat{x}}^2 v + \hat{\ell} \partial_{\hat{x}} \hat{\sigma}_a(\hat{M}) \tag{21c}$$

Almost all of these parameters are known (see Table 2), with the exception of $\hat{K}_{\text{CM}}$, which is given by

$$\hat{K}_{\text{CM}} = \frac{k_M^{\text{E}} C^{(\text{Tot})}}{k_M^{\text{off}} h}, \tag{22}$$

and describes the additional flux of myosin to the membrane from CDC-42 relative to the off rate.

Figure 11: Dimensionless myosin concentration at the uniform steady state as a function of the recruitment rate $\hat{K}_{\mathrm{CM}}$. The steady states are given in (24), and (using values in Table 2), are a function of only one unknown parameter, $\hat{K}_{\mathrm{CM}}$.

2.4.1 Steady states

There is a single uniform steady state $\hat{M} \equiv \hat{M}_0$ and $\hat{C} \equiv \hat{C}_0$ which is the solution to the (technically nonlinear) system of equations

$$\frac{k_C^{\mathrm{on}}}{h k_M^{\mathrm{off}}} \left(1 - \hat{C}_0\right) - \frac{k_C^{\mathrm{off}}}{k_M^{\mathrm{off}}} \hat{C} = 0 \tag{23a}$$

$$\left(\hat{K}_M^{\mathrm{on}} + \hat{K}_{\mathrm{CM}} \hat{C}_0\right) \left(1 - \hat{M}_0\right) - \hat{M}_0 = 0 \tag{23b}$$

The solution is, however, obvious because the solution for $\hat{C}_0$ can be obtained first

$$\hat{C}_0 = \frac{k_C^{\mathrm{on}}}{k_C^{\mathrm{on}} + h k_C^{\mathrm{off}}} \qquad \hat{M}_0 = \frac{\hat{K}_M^{\mathrm{on}} + \hat{K}_{\mathrm{CM}} \hat{C}_0}{\hat{K}_M^{\mathrm{on}} + \hat{K}_{\mathrm{CM}} \hat{C}_0 + 1}. \tag{24}$$

Thus, the steady state myosin concentration is a function of the amount of recruitment by CDC, which is the only unknown parameter in (24). Figure 11 shows that the uniform steady state transitions from 30% of myosin bound to the membrane to 100% bound at the uniform steady state as the dimensionless recruitment $\hat{K}_{\mathrm{CM}}$ increases from 0.1 to 1000. **We should therefore be able to constraint this parameter with experimental data – to discuss with Ed.**

2.4.2 Linear stability analysis

To understand how the stability of this model is different than that of myosin alone, we now perform a linear stability analysis about the steady state $\left(\hat{C}_0, \hat{M}_0\right)$ in (24). Because there are

multiple species in the equations, we'll modify our technique slightly from Section 2.3.1, letting

$$\hat{M} = \hat{M}_0 + \delta M = M_0 + \sum_k m_k(t)e^{2\pi ik} \qquad C = \hat{C}_0 + \delta C = \hat{C}_0 + \sum_k c_k(t)e^{2\pi ik}. \qquad (25)$$

Substituting this into the evolution equations (21) and using the steady state equations (23) gives evolution equations

$$m_k'(t) - \frac{\hat{M}_0\hat{\sigma}_0\,(2\pi k)^2\,\hat{\ell}\sigma_a'\left(\hat{M}_0\right)}{1 + \left(2\pi k\hat{\ell}\right)^2}m_k(t) = -\hat{D}_M\,(2\pi k)^2\,m_k(t) - m_k(t) + \hat{K}_{\mathrm{CM}}c_k(t)(1 - \hat{M}_0) \quad (26a)$$

$$c_k'(t) - \frac{\hat{C}_0\hat{\sigma}_0\,(2\pi k)^2\,\hat{\ell}\sigma_a'\left(\hat{M}_0\right)}{1 + \left(2\pi k\hat{\ell}\right)^2}m_k(t) = -\hat{D}_C\,(2\pi k)^2\,c_k(t) - \frac{k_C^{\mathrm{off}}}{k_M^{\mathrm{off}}}c_k(t) \qquad (26b)$$

$$\frac{d}{dt}\begin{pmatrix} m_k \\ c_k \end{pmatrix} = \begin{pmatrix} \dfrac{\hat{M}_0\hat{\sigma}_0\,(2\pi k)^2\,\hat{\ell}\sigma_a'\left(\hat{M}_0\right)}{1 + \left(2\pi k\hat{\ell}\right)^2} - (2\pi k)^2\,\hat{D}_M - 1 & \hat{K}_{\mathrm{CM}}(1 - \hat{M}_0) \\ \dfrac{\hat{C}_0\hat{\sigma}_0\,(2\pi k)^2\,\hat{\ell}\sigma_a'\left(\hat{M}_0\right)}{1 + \left(2\pi k\hat{\ell}\right)^2} & -(2\pi k)^2\,\hat{D}_C - k_C^{\mathrm{off}}/k_M^{\mathrm{off}} \end{pmatrix}\begin{pmatrix} m_k \\ c_k \end{pmatrix} \quad (26c)$$

The system is unstable when the determinant of this matrix is negative (at least one positive eigenvalue).

The two unknown parameters in the matrix (which we call $\boldsymbol{A}$) in (26c) are $\hat{\sigma}_0\sigma_a'\left(M_0\right)$ (related to the strength of the advective flows) and $\hat{K}_{\mathrm{CM}}$ (recruitment rate of myosin from CDC). To separate them, in Fig. 12 we plot the determinant of the matrix in (26c) as a function of k and two different parameters: $\hat{\sigma}_0\sigma_a'$ (which we vary independently of M_0) and $\hat{K}_{\mathrm{CM}}$. When the flow speed is fast enough, there exists a value of the recruitment rate $\hat{K}_{\mathrm{CM}}$ that leads to spontaneous polarization (in the plot at left it is $\hat{K}_{\mathrm{CM}} = 10$, where the $k = 3$ mode is the most unstable one). However, if the flow is too slow, there is no value of the myosin recruitment rate that leads to spontaneous polarization. This implies that even having all of the myosin in the system bound to the membrane is insufficient to trigger spontaneous polarization if the flow response is not high enough.

2.4.3 Inferring flow profile from experiments

Because we can measure the cortical velocity and myosin intensity, we can actually infer the function $\sigma_a(M)$ in dimensional units from the experimental data [13]. We in particular isolate the myosin intensity and flow speed during "late maintenance" phase in wild type embros [13, Fig. 1B(bottom)], plotting the results in the top panels of Fig. 13. In the top left plot, we plot the myosin intensity,
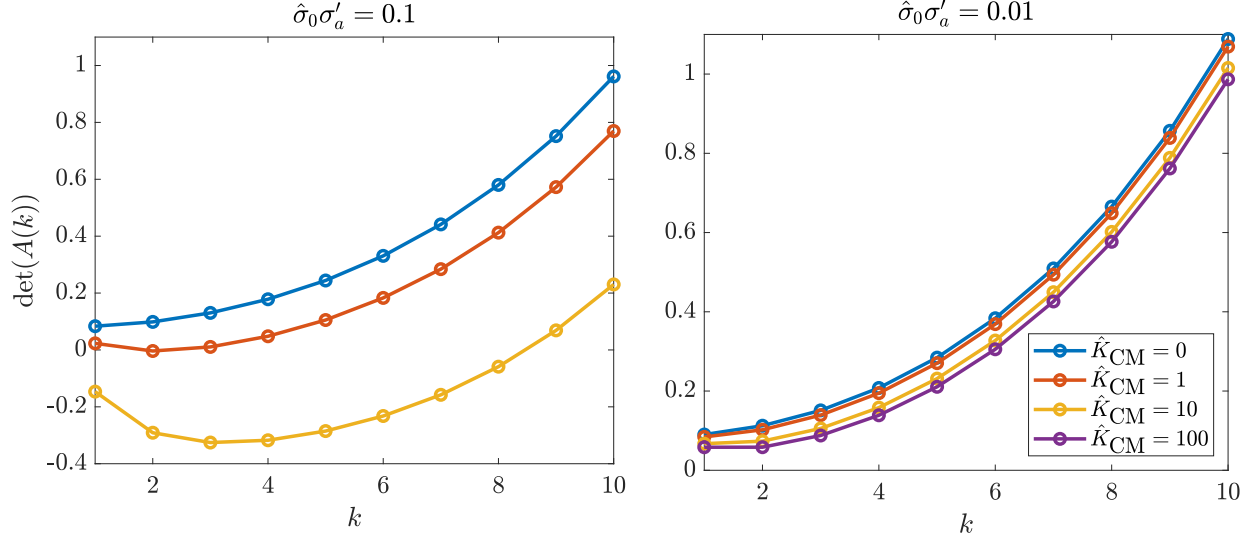
Figure 12: Stability of the myosin-CDC uniform steady state as a function of two unknown parameters: the flow $\hat{\sigma}_0\sigma'_a$ and the recruitment rate (of myosin by CDC) $\hat{K}_{\mathrm{CM}}$. To untangle the two parameters, we set $\hat{\sigma}_0\sigma'_a$ as an *independent* parameter here, dropping the functional dependence on $\hat{M}_0$, and plot the determinant of the matrix in (26c). A negative determinant implies an unstable uniform steady state.

normalized so that the maximum is roughly 1 and the minimum is 0. In the top right plot, we show the velocity in μm/s. In both cases, the data are plotted on $\hat{x} \in [0.25, 0.75]$, which corresponds to half of the embryo (one of the lines going from anterior to posterior end). We then periodically extend this data so that we fill the whole circumference $\hat{x} \in [0, 1]$; these are the blue lines in Fig. 13. Finally, to remove the noise from our measurements (e.g., the strange dips in the myosin concentration at the anteior and posterior pole), we fit the periodized version with a two-term (+constant) Fourier representation, which gives the red lines in Fig. 13.

To extract the stress profile from the smoothed velocity and myosin intensity, we consider a hybrid dimensional form of (13b)

$$\gamma v - \frac{\eta}{L^2}\partial_{\hat{x}}^2 v = \frac{1}{L}\partial_{\hat{x}}\sigma_a(M).$$

Let the Fourier series representation for $v(\hat{x}) = \sum_k \tilde{v}(k)\exp\left(2\pi i k\hat{x}\right)$, and likewise for $\hat{\sigma}_a$. Then, in Fourier space, the solution for σ_a is given by

$$\sigma_a(k) = \frac{\gamma + \eta/L^2\left(2\pi k\right)^2}{2\pi i k/L}\tilde{v}(k). \tag{27}$$

The $k = 0$ mode is undefined because σ_a only appears differentiated; we therefore set it such that the real space stress has a minimum value of zero.
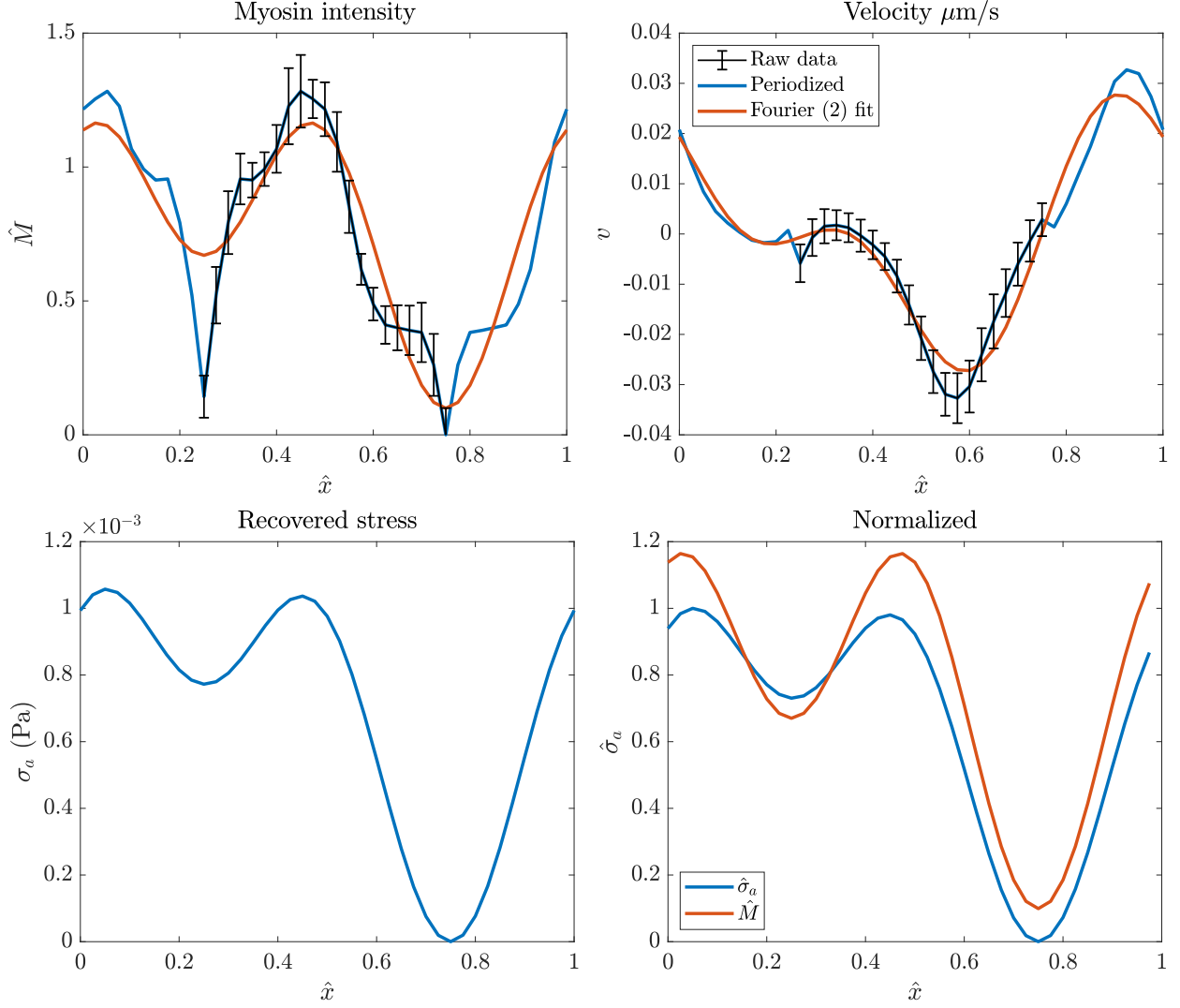
Figure 13: Extracting the velocity profile and active stress from experiments. Top: the experimental data for myosin intensity (left) and velocity in μm/s (right). We show the row data in black (which goes from anterior to posterior), the periodized version in blue, and a two-term (three terms if we include the constant) Fourier series representation in red. Bottom left: the recovered stress profile $\sigma_a(\hat{x})$ in dimensional units. Bottom right: comparing the recovered stress to the myosin intensity, after normalizing by $\sigma_0 = 0.0011$ Pa. It is clear that, roughly speaking, $\hat{\sigma}_a = \hat{M}$, or at least that this is a reasonable approximation.
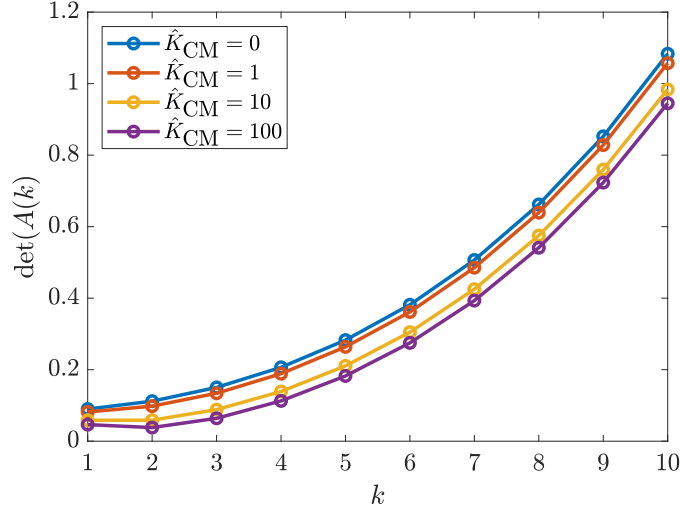
Figure 14: The dispersion relation (determinant of the matrix $\boldsymbol{A}$ in (26c)) under experimental conditions for maintenance (see Table 2). This system cannot spontaneously polarize for any value of the CDC-myosin recruitment strength $\hat{K}_{\mathrm{CM}}$.

We plug the parameters from Table 2 into (27) and show the resulting real space stress in the bottom left panel of Fig. 13. This is the dimensional stress σ_a, which allows us to read off the constant $\sigma_0 = 1.1 \times 10^{-3}$ Pa that controls the magnitude of the advective flows. In particular, the dimensionless parameter $\hat{\sigma}_0$ defined in (16) is seen to be equal to

$$\hat{\sigma}_0 = \left(\frac{\sigma_0/\sqrt{\eta\gamma}}{L k_M^{\mathrm{off}}} \right) = 0.014. \tag{28}$$

Finally, to obtain the functional form of the dimensionless stress $\hat{\sigma}_a$, in the bottom right panel of Fig. 13 we plot the dimensionless stress $\sigma_a/\hat{\sigma}_0$ (blue) together with the (filtered) myosin concentration $\hat{M}$ that we obtained initially from the experimental data. Because of a number of complicating factors, the values for $\hat{\sigma}_a(\hat{M})$ are ambiguous, as for instance $\hat{M} = 0.7$ gives two different values for $\hat{\sigma}_a$ depending on where we are in the embryo. Nevertheless, it is fairly clear that

$$\hat{\sigma}_a = \hat{M} \tag{29}$$

represents a good approximation to the stress, and so that is what we will use going forward.

Still to do: repeat this analysis with arp 2/3 knockouts

Now that we have extracted almost all of the key parameters, we repeat the dispersion/stability analysis of Fig. 12, but this time using our measured form of the stress $\sigma_a = \left(1.1 \times 10^{-3}\right) \hat{M}$. Figure 14 shows the determinant of the matrix $\boldsymbol{A}$ in (26c) as a function of the dimensionless myosin-CDC

recruitment rate $\hat{K}_{\mathrm{CM}}$. Even in the limit when CDC recruits all of the myosin, the flow speed is simply not strong enough to form its own patterns. Thus, our system *cannot* spontaneously polarize, which suggests that the amplification of weak asymmetries comes from intrinsic *bistability* rather than instability of the uniform steady state.

3 Complete model of maintenance phase rescue

3.1 Model of PAR-2 and PAR-3 with myosin

Let's now add myosin to the model of PAR-2 and PAR-3 that we formulated in (6). Myosin enters here as an advective flow for each of the proteins, then has its own constitutive equation. In Section 2.4, we showed that the only role of CDC-42 is to recruit myosin to the membrane. Based on this, we don't include CDC-42 in this model, but assume that its effect can be captured by increasing the on rate of myosin to get a larger total amount. With these assumptions in mind, the full dimensionless model is given by

$$\partial_{\hat{t}}\hat{A}_1 + \hat{\sigma}_0\partial_{\hat{x}}\left(\hat{v}\hat{A}_1\right) = \hat{D}_A\partial_{\hat{x}}^2\hat{A}_1 + \hat{K}_A^{\mathrm{on}}\left(1 + \hat{K}_A^+ f_A^+\left(\hat{A}_1(x) + 2\hat{A}_n(x)\right)\right)\left(1 - \int_0^1\left(\hat{A}_1(x) + 2\hat{A}_n(x)\right)d\hat{x}\right)$$
$$-\hat{K}_A^{\mathrm{off}}\hat{A}_1 + 2\hat{K}_A^{\mathrm{dp}}\hat{A}_n - 2\hat{K}_A^{\mathrm{p}}\hat{A}_1^2 \tag{30a}$$

$$\partial_{\hat{t}}\hat{A}_n + \hat{\sigma}_0\partial_{\hat{x}}\left(\hat{v}\hat{A}_n\right) = \hat{K}_A^{\mathrm{p}}\hat{A}_1^{\,2} - \hat{K}_A^{\mathrm{dp}}\hat{A}_n - \frac{r_{\mathrm{PA}}P^{(\mathrm{Tot})}}{k_A^{\mathrm{dp}}}\hat{P}\hat{A}_n \tag{30b}$$

$$\partial_{\hat{t}}\hat{P} + \hat{\sigma}_0\partial_{\hat{x}}\left(\hat{v}\hat{P}\right) = \hat{D}_P\partial_{\hat{x}}^2\hat{P} + \hat{K}_P^{\mathrm{on}}\left(1 - \int_0^1\hat{P}(\hat{x})\,d\hat{x}\right) - \hat{K}_P^{\mathrm{off}}\hat{P} - \frac{r_{\mathrm{AP}}A^{(\mathrm{Tot})}}{k_A^{\mathrm{dp}}}\left(\hat{A}_1 + 2\hat{A}_n\right)\hat{P} \tag{30c}$$

$$\partial_{\hat{t}}\hat{M} + \hat{\sigma}_0\partial_{\hat{x}}\left(\hat{v}\hat{M}\right) = \hat{D}_M\partial_{\hat{x}}^2\hat{M} + \hat{K}_M^{\mathrm{on}}\left(1 - \int_0^1\hat{M}(x)\,dx\right) - \left(\hat{K}_M^{\mathrm{off}} + \frac{r_{\mathrm{PM}}P^{(\mathrm{Tot})}}{k_A^{\mathrm{dp}}}\hat{P}\right)\hat{M} \tag{30d}$$

$$\hat{v} = \hat{\ell}^2\partial_{\hat{x}}^2 v + \hat{\ell}\partial_{\hat{x}}\hat{\sigma}_a(\hat{M}) \tag{30e}$$

$$\hat{D}_A = \frac{D_A}{L^2 k_A^{\mathrm{dp}}}, \quad \hat{K}_A^{\mathrm{on}} = \frac{k_A^{\mathrm{on}}}{k_A^{\mathrm{dp}}h}, \hat{K}_A^{\mathrm{off}} = \frac{k_A^{\mathrm{off}}}{k_A^{\mathrm{dp}}}, \quad \hat{K}_A^{\mathrm{dp}} = 1, \quad \hat{K}_A^{\mathrm{p}} = \frac{k_A^{\mathrm{p}}A^{(\mathrm{Tot})}}{k_A^{\mathrm{dp}}}, \quad \hat{K}_A^+ = \frac{k_A^+}{k_A^{\mathrm{on}}}$$

$$\hat{D}_P = \frac{D_P}{L^2 k_A^{\mathrm{dp}}}, \quad \hat{K}_P^{\mathrm{on}} = \frac{k_P^{\mathrm{on}}}{k_A^{\mathrm{dp}}h}, \quad \hat{K}_P^{\mathrm{off}} = \frac{k_P^{\mathrm{off}}}{k_A^{\mathrm{dp}}}, \quad \hat{\sigma}_0 = \left(\frac{\sigma_0/\sqrt{\eta\gamma}}{Lk_A^{\mathrm{dp}}}\right) \tag{30f}$$

$$\hat{D}_M = \frac{D_M}{k_A^{\mathrm{dp}}L^2}, \quad \hat{K}_M^{\mathrm{on}} = \frac{k_M^{\mathrm{on}}}{hk_A^{\mathrm{dp}}}, \quad \hat{K}_M^{\mathrm{off}} = \frac{k_M^{\mathrm{off}}}{k_A^{\mathrm{dp}}}, \quad \hat{\ell} = \frac{\sqrt{\eta/\gamma}}{L} \quad v = \hat{v}\frac{\sigma_0}{\sqrt{\eta\gamma}}.$$

Our key assumption here is that the posterior PAR-2 inhibits myosin activity through the reaction coefficient r_{PM} (units μm/s). Recalling our previous study of PAR-2 and PAR-3 in Section 1.3, we saw there that for strong enough mutual inhibition of the two proteins, the intrinsic bistability of
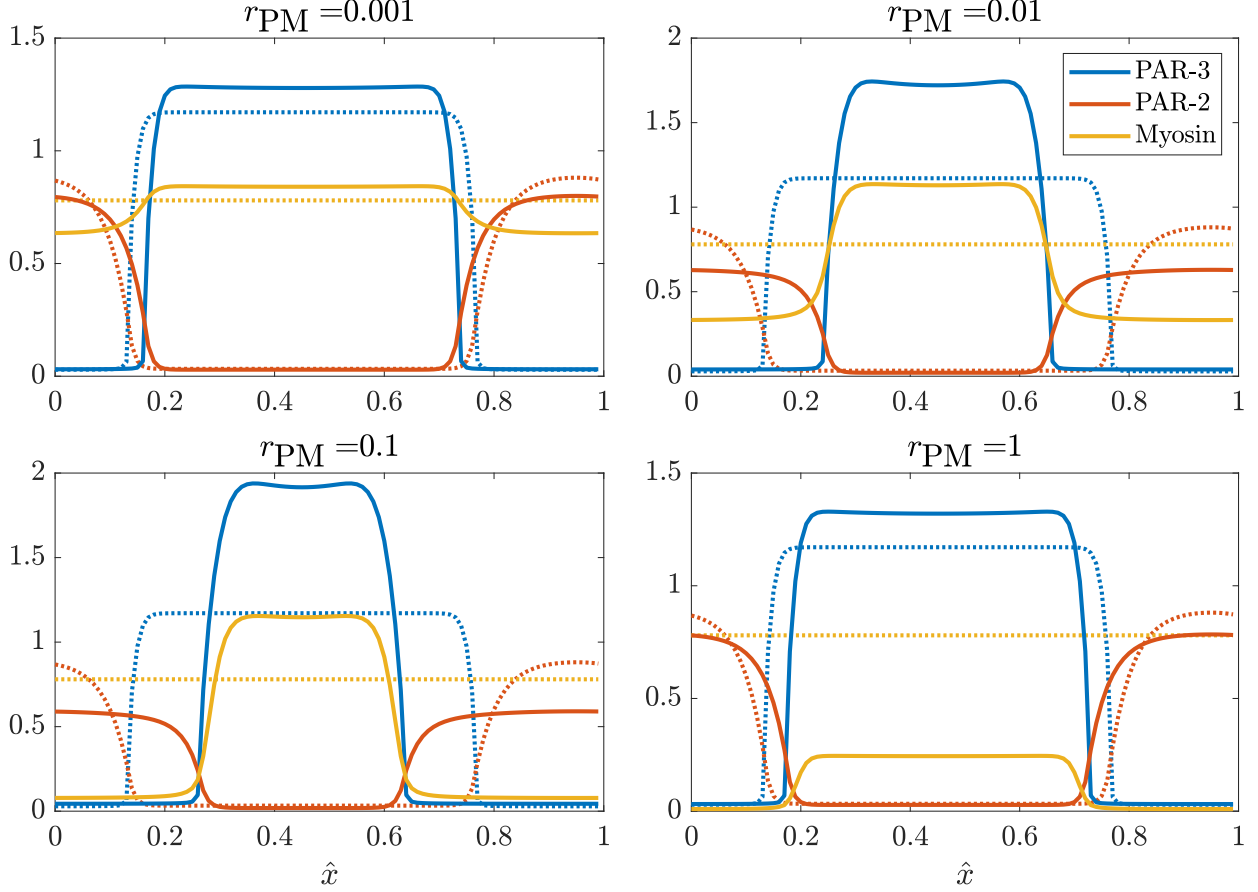
Figure 15: Fixing $r_{AP} = 10^{-2}$ and changing the degree to which PAR-2 inhibits myosin in the model (30). The dotted lines show the steady state when $r_{PM} = 0$ (blue for PAR-3, red for PAR-2, yellow for myosin), while the solid lines show the steady state with the value of r_{PM} indicated in the title.

PAR-3 can combine with mutual inhibition of PAR-2 to set up two mutually exclusive domains of enriched PAR-2 and PAR-3 (respectively).

But can we use myosin as a means to shift the boundary? Figure 15 shows that indeed we can. Here we consider the same parameters as given in Table 1, but add myosin with the parameters given in Table 2. In order to get more bound myosin, we increase to $k_M^{on} = 2$ μm/s (a factor of 10 relative to the value reported in [5], which is based on fitting a different model). The dotted lines in each plot show the steady state with $r_{PM} = 0$, so that we can see how adding PAR-2 inhibition of myosin shifts the boundary. Starting with $r_{PM} = 10^{-3}$ up to $r_{PM} = 0.1$, we see a PAR-3 domain which constantly shrinks. If we raise the inhibition high enough, we see less myosin, which doesn't produce as much flow. The limit $r_{PM} \to \infty$ therefore gives the same behavior as $r_{PM} = 0$, since there is no flow in either case.

What stops the boundary from expanding? The boundary between the domains expands when there is enough flow of PAR-2 so as to push PAR-3 from its higher steady state to its lower one. The flow of PAR-2 is linked to the gradient in myosin, which in turn depends on the gradient of PAR-2. The amount of PAR-2 comes from cytoplasm. The flow is Cytoplasmic PAR-2 depleted $\rightarrow$ less on flux $\rightarrow$ less myosin $\rightarrow$ boundary eventually stops moving. In the case when there is unlimited cytoplasmic PAR-2, the limit then becomes cytoplasmic PAR-3. The on rate keeps getting higher as we deplete PAR-3, until it outcompetes everything.

3.1.1 Comparison with experiments

We now attempt an honest comparison with the experimental data. We have already seen that there are two unknown parameters in doing so: the inhibition strengths r_{AP} (PAR-2/PAR-3 inhibition) and r_{PM} (PAR-2/myosin inhibition). To select them, we choose an initial condition where 10% of the embryo is devoid of PAR-3. In Fig. 16 (top left), we then select $r_{\mathrm{AP}} = 0.002$ so that, without myosin flows, the posterior domain expands to 25% of the embryo length [16, Fig. 5B] (see Section 1.3 for an explanation of this). Finally, we select $r_{\mathrm{PM}} = 0.01$, so that the flow yields a posterior/anterior domain of roughly equal size (top right of Fig. 16).

In the bottom panel of Fig. 16, we compare the myosin and flow profiles from the model to the experimental data. The dynamics in the posterior half of the embryo look similar, with flow becoming more negative and myosin intensity increasing as we move from right ($\hat{x} \approx 0.75$) to $\hat{x} = 0.4$. However, the key difference in the flow profile is the lack of a stalled region in the anterior. In experiments, we see that the flow essentially stalls around $\hat{x} = 0.4$ (or 20% of the egg length from the anterior pole), whereas we see a stall point at the anterior *pole* in our model. In this next section, we attempt to rescue this by accounting for branched actin.

3.1.2 Local zone of myosin inhibition

A better match to the experimental data can be obtained by assuming a local zone of myosin inhibition near the anterior cap. For now we do this by doubling the off rate when $0.2 \leq \hat{x} \leq 0.3$. We again set $r_{\mathrm{AP}} = 0.002$ and $r_{\mathrm{PM}} = 0.01$ to try to match experiments. As shown in Fig. 17, this crude approximation is a better match to the experimental data. We note that this is not intended to be the final word, but rather demonstrate that we need something at the anterior cap that inhibits myosin. Such an agent would successfully allow us to reproduce the experimental flow profile.
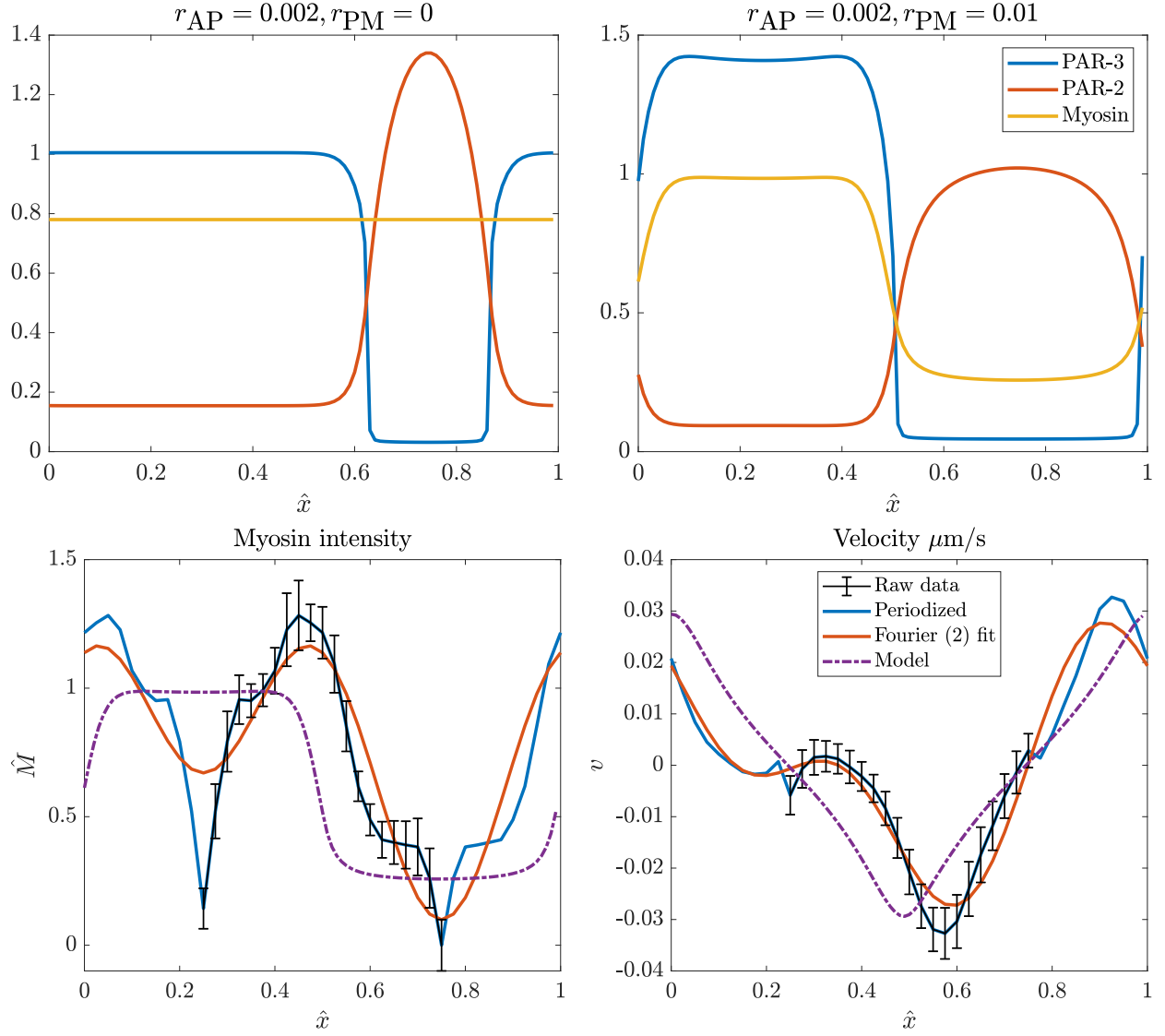
Figure 16: Comparing simulations to experimental data. Top panel: setting the inhibition strengths based on experimental conditions. We choose $r_{\mathrm{AP}} = 0.002$, so that in the absence of flows the PAR-3 domain takes up roughly 75% of the embryo [16, Fig. 5B]. We then set $r_{\mathrm{PM}} = 0.01$, so that flows take us to a roughly 50/50 split. The initial condition in both cases is 10% of the embryo enriched with PAR-2, and we show steady states at $\hat{t} = 200$. Bottom: comparing the myosin intensity and velocity to the experiments in wild-type embryos [13]. Results from simulations (steady states) are shown in dotted purple lines.
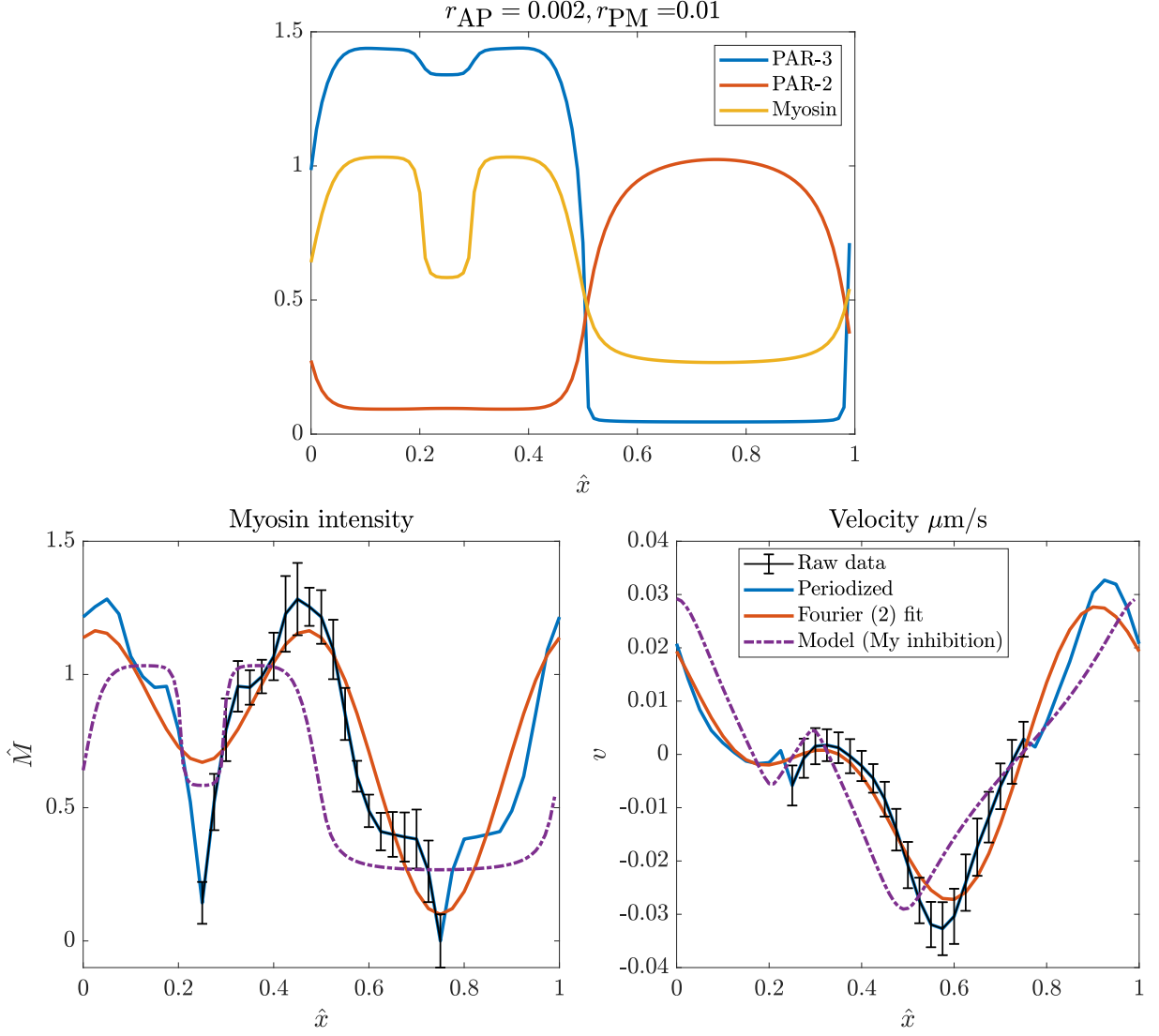
Figure 17: Comparing simulations to experimental data when we inhibit myosin locally in the anterior cap. We again set $r_{\text{AP}} = 0.002$ and $r_{\text{PM}} = 0.01$ to try to match experiments, but double the rate of myosin detachment over $0.2 \leq \hat{x} \leq 0.3$. This crudely gives the flow on the anterior half that we are looking for.

3.2 Accounting for branched actin

1. Flow profile in embryos without arp 2/3. Does it resemble simulation? If yes, then arp 2/3 is reponsible for the cap and stalling.

2. Model where high myosin concentration also gives branched actin. Figure that out later.

3. IN FINAL SIMULATIONS MAKE SURE THINGS ARE CONVERGED $N = 100$ NOT ENOUGH FOR SURE! $N = 1000$ is really nice! This is first order advection so need lot of points.

References

[1] Tom Bland, Nisha Hirani, David Briggs, Riccardo Rossetto, KangBo Ng, Neil Q McDonald, David Zwicker, and Nathan W Goehring. Optimized dimerization of the par-2 ring domain drives cooperative and selective membrane recruitment for robust feedback-driven cell polarization. *bioRxiv*, pages 2023–08, 2023.

[2] Justin S Bois, Frank Jülicher, and Stephan W Grill. Pattern formation in active fluids. *Biophysical Journal*, 100(3):445a, 2011.

[3] Adriana T Dawes and Edwin M Munro. Par-3 oligomerization may provide an actin-independent mechanism to maintain distinct par protein domains in the early caenorhabditis elegans embryo. *Biophysical journal*, 101(6):1412–1422, 2011.

[4] Nathan W Goehring, Philipp Khuc Trong, Justin S Bois, Debanjan Chowdhury, Ernesto M Nicola, Anthony A Hyman, and Stephan W Grill. Polarization of par proteins by advective triggering of a pattern-forming system. *Science*, 334(6059):1137–1141, 2011.

[5] Peter Gross, K Vijay Kumar, Nathan W Goehring, Justin S Bois, Carsten Hoege, Frank Jülicher, and Stephan W Grill. Guiding self-organized pattern formation in cell polarity establishment. *Nature physics*, 15(3):293–300, 2019.

[6] Jacob Halatek, Fridtjof Brauns, and Erwin Frey. Self-organization principles of intracellular pattern formation. *Philosophical Transactions of the Royal Society B: Biological Sciences*, 373(1747):20170107, 2018.

[7] Rukshala Illukkumbura, Nisha Hirani, Joana Borrego-Pinto, Tom Bland, KangBo Ng, Lars Hubatsch, Jessica McQuade, Robert G Endres, and Nathan W Goehring. Design principles for selective polarization of par proteins by cortical flows. *Journal of Cell Biology*, 222(8), 2023.

[8] Charles F Lang, Alexander Anneken, and Edwin Munro. Oligomerization and feedback on membrane recruitment stabilize par-3 asymmetries in c. elegans zygotes. *bioRxiv*, pages 2023–08, 2023.

[9] Charles F Lang and Edwin Munro. The par proteins: from molecular circuits to dynamic self-stabilizing cell polarity. *Development*, 144(19):3405–3416, 2017.

[10] Charles F Lang and Edwin M Munro. Oligomerization of peripheral membrane proteins provides tunable control of cell surface polarity. *Biophysical Journal*, 121(23):4543–4559, 2022.

[11] Alex Mogilner, Jun Allard, and Roy Wollman. Cell polarity: quantitative modeling as a tool in cell biology. *Science*, 336(6078):175–179, 2012.

[12] François B Robin, William M McFadden, Baixue Yao, and Edwin M Munro. Single-molecule analysis of cell surface dynamics in caenorhabditis elegans embryos. *Nature methods*, 11(6):677–682, 2014.

[13] Anne Sailer, Alexander Anneken, Younan Li, Sam Lee, and Edwin Munro. Dynamic opposition of clustered proteins stabilizes cortical polarity in the c. elegans zygote. *Developmental cell*, 35(1):131–142, 2015.

[14] Filipe Tostevin and Martin Howard. Modeling the establishment of par protein polarity in the one-cell c. elegans embryo. *Biophysical journal*, 95(10):4512–4522, 2008.

[15] Philipp Khuc Trong, Ernesto M Nicola, Nathan W Goehring, K Vijay Kumar, and Stephan W Grill. Parameter-space topology of models for cell polarity. *New Journal of Physics*, 16(6):065009, 2014.

[16] Seth Zonies, Fumio Motegi, Yingsong Hao, and Geraldine Seydoux. Symmetry breaking and polarization of the c. elegans zygote by the polarity protein par-2. *Development*, 137(10):1669–1677, 2010.